



HAL
open science

Hydrostatic Interfaces in Bodies With Nonhydrostatic Lithospheres

Mark Wieczorek, Mikael Beuthe, Attilio Rivoldini, Tim van Hoolst

► **To cite this version:**

Mark Wieczorek, Mikael Beuthe, Attilio Rivoldini, Tim van Hoolst. Hydrostatic Interfaces in Bodies With Nonhydrostatic Lithospheres. *Journal of Geophysical Research. Planets*, 2019, 124 (5), pp.1410-1432. 10.1029/2018JE005909 . hal-02324427

HAL Id: hal-02324427

<https://hal.science/hal-02324427>

Submitted on 26 Jun 2020

HAL is a multi-disciplinary open access archive for the deposit and dissemination of scientific research documents, whether they are published or not. The documents may come from teaching and research institutions in France or abroad, or from public or private research centers.

L'archive ouverte pluridisciplinaire **HAL**, est destinée au dépôt et à la diffusion de documents scientifiques de niveau recherche, publiés ou non, émanant des établissements d'enseignement et de recherche français ou étrangers, des laboratoires publics ou privés.

Hydrostatic Interfaces in Bodies With Nonhydrostatic Lithospheres

Mark A. Wieczorek¹ , Mikael Beuthe² , Attilio Rivoldini² , and Tim Van Hoolst² 

¹Université Côte d'Azur, Observatoire de la Côte d'Azur, CNRS, Laboratoire Lagrange, Nice, France, ²Royal Observatory of Belgium, Brussels, Belgium

Key Points:

- The terrestrial planets and moons are not in hydrostatic equilibrium and contain mass anomalies in their lithospheres
- The lithosphere generates a gravitational potential that affects the shape of deep interfaces that are hydrostatic
- Hydrostatic interfaces deviate by about 10% for Mars with respect to those for an entirely fluid planet and even more for the Moon

Correspondence to:

M. A. Wieczorek,
mark.wieczorek@oca.eu

Citation:

Wieczorek, M. A., Beuthe, M., Rivoldini, A., & Van Hoolst, T. (2019). Hydrostatic interfaces in bodies with nonhydrostatic lithospheres. *Journal of Geophysical Research: Planets*, 124. <https://doi.org/10.1029/2018JE005909>

Received 23 DEC 2018

Accepted 21 MAR 2019

Accepted article online 1 APR 2019

Author Contributions

Conceptualization: Mark A. Wieczorek

Data curation: Mark A. Wieczorek

Methodology: Mark A. Wieczorek, Mikael Beuthe, Attilio Rivoldini

Software: Mark A. Wieczorek

Validation: Mark A. Wieczorek, Mikael Beuthe, Attilio Rivoldini

Writing - Original Draft: Mark A. Wieczorek, Mikael Beuthe, Attilio Rivoldini

Formal Analysis: Mark A. Wieczorek

Investigation: Mark A. Wieczorek

Resources: Mark A. Wieczorek

Visualization: Mark A. Wieczorek

Writing - review & editing: Mark A. Wieczorek, Mikael Beuthe, Attilio Rivoldini

Abstract Below the lithospheres of the terrestrial planets, dwarf planets, and moons, density interfaces adjust over geologic time to align with surfaces of constant gravitational potential. It is well known that the shape of such hydrostatic surfaces is controlled by the pseudo-rotational potential, tidal potential, and the induced potential of nonspherical density interfaces in the body. When a lithosphere is present, however, additional gravitational terms must be considered that arise from, for example, surface relief and crustal thickness variations. A first-order formalism is presented for calculating the shape of hydrostatic density interfaces beneath the lithosphere when the gravity field and surface shape of the body are known. Using an arbitrary discretized density profile, the shapes are obtained by solving a simple matrix equation. As examples, lithospheric gravity anomalies account for about 10% of the relief along hydrostatic interfaces in Mars, whereas for the Moon, the lithospheric gravity is the dominant contributor to the core shape. Spherical harmonic degree-1 mass anomalies in the lithosphere generate degree-1 relief along the core-mantle boundary, and for Mars and the Moon, the core is offset from the center of mass of the body by about 90 m. The moments of inertia of the core of these bodies are also misaligned with respect to the principal moments of the entire body. An improved crustal thickness map of Mars is constructed that accounts for gravity anomalies beneath the lithosphere, and the consequences of core relief on the Martian free core nutation are quantified.

Plain Language Summary The shapes of the solid planets and moons are largely hydrostatic and are determined by their rotation rate. If the body has gravity anomalies that arise from within a rigid lithosphere, these will act to perturb the shape of hydrostatic density interfaces beneath the lithosphere, such as the core-mantle boundary. We present a method to compute the shape of density interfaces beneath the lithosphere when the gravity field of the body is known. As examples of our technique, we compute the shape of the core-mantle boundary for Mars and the Moon, both of which are shown to have important contributions that arise from the lithosphere. We also generate a new crustal thickness map that accounts for gravity anomalies generated beneath the lithosphere.

1. Introduction

The problem of calculating the shape and gravity field of a rotating hydrostatic body subject to tides is a classic one that goes back to the work of Clairaut (1743). Though the problem involves only a simple force balance, in practice, the general solution for a rapidly rotating body with nonnegligible flattening is a difficult one. A first-order treatment is often sufficient for many problems in planetary science, but higher-order methods can become necessary when treating fast-rotating objects such as Jupiter. Several methods based on different approaches have been developed to solve for the shape of density interfaces within a fluid object that take into account nonlinear effects to both second and higher order, with notable examples including the work of Kopal (1960), Lanzano (1982), Zharkov and Trubitsyn (1978), Chandrasekhar (1969), and Hubbard (2013). Applications of these techniques are common in planetary science (e.g., Chambat et al., 2010; Ermakov et al., 2017; Nakiboglu, 1982; Rambaux et al., 2015; Wisdom & Hubbard, 2016).

It is quite natural to invoke the hypothesis of hydrostatic equilibrium for objects that have no surface strength, such as the Sun and the giant planets of our solar system. When viewed from afar, even solid bodies appear to be approximately in hydrostatic equilibrium, with the flattening depending directly on the rotation rate and interior density profile (e.g., Iess et al., 2010; Park et al., 2016; Schubert et al., 2004; Smith et al., 1999). Nevertheless, as one approaches the terrestrial planets, geologic processes lead to the development of

mass anomalies in the strong outer portion of the body, and these mass anomalies create large gravitational anomalies (for a review, see Wiczorek, 2015). This strong outer portion of the planet, referred to as the lithosphere, can support deviatoric stresses over geologic time, and thus, these mass anomalies will not be in hydrostatic equilibrium. In contrast, the deep interiors of the terrestrial planets, where the temperatures are elevated and rocks deform by creeping viscous flow, are expected to be in hydrostatic equilibrium. As is the case with rotational and tidal potentials, the gravitational potential of mass anomalies in the lithosphere should play a role in determining the shapes of hydrostatic surfaces at depth.

A few studies have recognized the importance of accounting for lithospheric gravitational anomalies when calculating the hydrostatic shape of the core of a planet. In a study by Meyer and Wisdom (2011), long-wavelength lithospheric gravitational anomalies of spherical harmonic degree 2 and order 0 were included when calculating the hydrostatic shape of the core of the Moon. It was found that the core flattening should be about 10 times larger than that predicted for an entirely fluid planet. This excess flattening is consistent with analyses of lunar laser ranging (LLR) data, and Dumberry and Wiczorek (2016) showed that this could have an important influence on the rotational state of a putative solid inner core. In a study by Le Bars et al. (2011), the lithospheric degree 2 and order 2 gravity field was used to determine the equatorial ellipticity of the lunar core, and this was found to be about 5 times larger than that for an entirely fluid planet. With the computed ellipticity, short-lived episodes of nonsynchronous rotation and/or librations of the mantle (generated by impacts) were shown to be sufficient to excite inertial instabilities in the fluid core, potentially powering a short-lived dynamo. Dumberry et al. (2013) computed the hydrostatic ellipticity of the core of Mercury and showed that this affected the librational signature of the planet. A few studies have considered the shapes of deep hydrostatic interfaces in Titan, Enceladus, and Dione when inverting the observed gravity field and librations for ice shell thickness (Baland et al., 2014; Beuthe et al., 2016; Hoolst et al., 2016; Lefevre et al., 2014). Finally, we note that Zharkov et al. (2009) considered the effects of lithospheric mass anomalies on the degree-2 shape of the Martian core but by using an approach that considered elastic deformations.

In this study we develop a first-order technique for computing the shape of density interfaces beneath the lithosphere of a planet when the gravity field of the body is known. The approach is to calculate the potential on discrete hydrostatic density interfaces in the object, accounting explicitly for the gravitational potential that results from rotation, tides, and mass anomalies in the lithosphere. The lithospheric anomalies are modeled as being nonhydrostatic and as arising from two sources: one that is a result of relief at the surface and another that results from mass anomalies at a specified depth within the lithosphere (typically, the base of the crust). The relief along all interfaces is solved simultaneously by requiring the potential to be constant along hydrostatic interfaces and by requiring the sum of the gravitational attraction of all interfaces to be equal to the observed value. The problem can be expressed as a set of linear equations, and the solution is determined by solving a simple matrix equation, in contrast to Clairaut's second-order differential equation. Our approach is shown to be more accurate than approaches that are first order in the ratio of centrifugal to gravitational forces due to the inclusion of an extra term in the rotational potential. Finally, at least for the case of Mars and the Moon, we demonstrate that the magnitude of higher-order terms is negligible in comparison to nonhydrostatic lithospheric effects.

In this paper, we first describe the methodology for computing the relief of hydrostatic interfaces beneath the lithosphere. This includes calculating the gravitational potential along an interface, requiring the potential to be constant along hydrostatic interfaces, and also requiring that the predicted gravity matches the observations. Following this, we validate our technique by comparing our results for an entirely fluid body with those obtained from a second- and third-order theory of figures for Mars and Ceres. Next, we demonstrate the utility of our approach for several problems related to Mars and the Moon. For Mars, we first compute the relief along hydrostatic density interfaces in both the core and mantle. Then using these results, we compute a new global crustal thickness map of the planet that accounts for the gravitational attraction of hydrostatic interfaces beneath the lithosphere. These global crustal thickness models will benefit from data that are being collected by the InSight seismometer (Lognonné et al., 2019; Smrekar et al., 2019). Following this, we then quantify how the lithospheric mass anomalies affect the free core nutation period of Mars that will be measured by the InSight spacecraft (Folkner et al., 2018). For the Moon, we compute the shape of the core-mantle interface, showing that the core is not aligned with the principal axes of the Moon and that the core is slightly offset from its center of mass. These results have implications for the interpretation of lunar

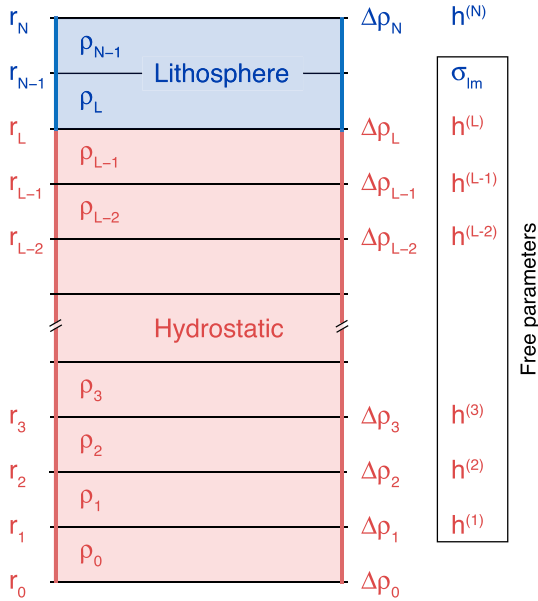


Figure 1. Schematic illustration of the interior structure of the body. r_i denotes the interfaces of constant density layers, ρ_i is the density between two interfaces, $\Delta\rho_i$ is the density contrast at interface i , and $h^{(i)}$ is the relief of interface i . r_0 corresponds to the center of the planet, r_L corresponds to the shallowest interface that is entirely hydrostatic, r_N is the radius of the surface, and the index L corresponds to $N - 2$. In practice, r_L corresponds to $r_N - T$, where T is the maximum thickness of the lithosphere. A nonhydrostatic mass sheet σ_{lm} is placed at r_{N-1} within the lithosphere. The radii r_i , densities ρ_i , density contrasts $\Delta\rho_i$, and surface relief $h^{(N)}$ are all treated as known quantities, whereas $h^{(1)}$ to $h^{(L)}$ and σ_{lm} are to be determined.

and above, U^- , the observation point. U_{rot} corresponds to the contribution from the rotational potential, and U_{lith} is the potential derived from the nonhydrostatic lithosphere.

To facilitate the derivations of the above terms, the planet will be described by a spherically symmetric reference 1-dimensional density profile that is composed of N constant density layers ρ_i bounded by constant radii r_i and r_{i+1} (see Figure 1):

$$\rho(r) = \rho_i \quad \text{for} \quad r_i \leq r < r_{i+1}, \quad (2)$$

where the center and surface of the body correspond to r_0 and r_N , respectively. Each interface i will be perturbed from this reference state, with its shape given by

$$r^{(i)}(\theta, \phi) = r_i + \sum_{l=1}^{\infty} \sum_{m=-l}^l h_{lm}^{(i)} Y_{lm}(\theta, \phi), \quad (3)$$

where Y_{lm} is the real spherical harmonic of degree l and order m , normalized using the geodesy 4π convention (e.g., Wiczonek & Meschede, 2018), and h_{lm} is the associated spherical harmonic coefficient. Each interface i is also associated with a density contrast

$$\Delta\rho_i = \rho_{i-1} - \rho_i. \quad (4)$$

Given that the density of the atmosphere above the surface of a terrestrial body is negligible when compared to rock, we make the approximation that ρ_N is 0 and set $\Delta\rho_N = \rho_{N-1}$. Furthermore, for the first interface at the center of the planet, we define $\Delta\rho_0 = 0$. For brevity of notation, the angular dependence of all functions will be dropped when there is no confusion.

The planet will be assumed to be in hydrostatic equilibrium for all interfaces where $i \leq L = N - 2$. Above this, there will be three-dimensional variations in density within the lithosphere that result from surface

laser ranging data, as well as the generation of a dynamo in its past. Finally, we conclude by summarizing the main results of the paper.

2. Hydrostatic Relief With a Lithosphere

In this section, the relief along hydrostatic interfaces within a body is computed when the object contains a nonhydrostatic lithosphere. In the first subsection, expressions are given for the gravitational potential along arbitrary density interfaces in the body. In the second subsection, the assumption of hydrostatic equilibrium is invoked, which requires that the gravitational potential be constant along each hydrostatic interface. This allows to write the coupled equations in matrix form, allowing for a simple resolution of the problem. In the third section, we introduce a correction for the degree-4 terms that are a result of the large amplitudes of the degree-2 shape of the planet. Finally, we describe how this approach can be modified when tidal potentials for a synchronously locked satellite are considered. Our methodology treats perturbations in relief with respect to a reference sphere to first order and retains all terms that are linear in the spherical harmonic coefficients of the relief. The main results of this section are given by equations (31)–(34).

2.1. Gravitational Potential Along an Interface

In a reference frame that is fixed to a rotating body, the potential along an interface $r(\theta, \phi)$ can be decomposed into several components:

$$U = U_0^+ + U_0^- + U^+ + U^- + U_{\text{rot}} + U_{\text{lith}}. \quad (1)$$

The first two terms correspond to the gravitational potential of the unperturbed spherical symmetric reference state from mass below, U_0^+ , and above, U_0^- , an arbitrary observation point. The next two terms correspond to the contribution from relief along each density interface below, U^+ ,

and above, U^- , the observation point. U_{rot} corresponds to the contribution from the rotational potential, and U_{lith} is the potential derived from the nonhydrostatic lithosphere.

To facilitate the derivations of the above terms, the planet will be described by a spherically symmetric reference 1-dimensional density profile that is composed of N constant density layers ρ_i bounded by constant radii r_i and r_{i+1} (see Figure 1):

$$\rho(r) = \rho_i \quad \text{for} \quad r_i \leq r < r_{i+1}, \quad (2)$$

where the center and surface of the body correspond to r_0 and r_N , respectively. Each interface i will be perturbed from this reference state, with its shape given by

$$r^{(i)}(\theta, \phi) = r_i + \sum_{l=1}^{\infty} \sum_{m=-l}^l h_{lm}^{(i)} Y_{lm}(\theta, \phi), \quad (3)$$

where Y_{lm} is the real spherical harmonic of degree l and order m , normalized using the geodesy 4π convention (e.g., Wiczonek & Meschede, 2018), and h_{lm} is the associated spherical harmonic coefficient. Each interface i is also associated with a density contrast

$$\Delta\rho_i = \rho_{i-1} - \rho_i. \quad (4)$$

Given that the density of the atmosphere above the surface of a terrestrial body is negligible when compared to rock, we make the approximation that ρ_N is 0 and set $\Delta\rho_N = \rho_{N-1}$. Furthermore, for the first interface at the center of the planet, we define $\Delta\rho_0 = 0$. For brevity of notation, the angular dependence of all functions will be dropped when there is no confusion.

The planet will be assumed to be in hydrostatic equilibrium for all interfaces where $i \leq L = N - 2$. Above this, there will be three-dimensional variations in density within the lithosphere that result from surface

topography, lateral variations in crustal thickness, and lateral variations in crustal and upper mantle density. The thickness of the lithosphere of a planet is not constant, and in practice, the interface r_L will be defined as $r_N - T$, where T is the maximum lithospheric thickness. The interface r_L could be thought of as the uppermost interface of the asthenosphere that is entirely hydrostatic. For simplicity, we will sometimes refer to everything above the interface r_L as being the “lithosphere,” but we emphasize that some regions above this interface could in fact be hydrostatic where the real lithospheric thickness is thinner than T .

The lithospheric signal will be treated as being derived from two separate interfaces. The first interface corresponds to the known surface relief at average radius r_N , where a constant density contrast of $\Delta\rho_N = \rho_{N-1}$ will be assumed. The remainder of the gravity signal will be treated as arising from a single mass sheet at an average radius r_{N-1} that lies between the surface and r_L and which encompasses all other unknown variations in density within the lithosphere. In practice, the average depth of this interface will be chosen to be equal to the average thickness of the crust of the body.

Before continuing, we note that lateral variations in density could in fact exist in the deep mantle and that nonhydrostatic relief could potentially exist at the core-mantle boundary (e.g., McKinnon, 2013; Wu & Wahr, 1997). For example, mantle convection could give rise to three-dimensional lateral variations in mantle temperature and mantle composition (e.g., Romanowicz, 2003), as well as dynamic topography at the core-mantle boundary (e.g., Defraigne et al., 2001). Unfortunately, beyond Earth, we have few (if any) constraints on the three-dimensional interior structure of the other planets and moons. Thus, in the spirit of the first-order analysis that follows and combined with a paucity of constraints on the interior structures of the terrestrial planets and moons, we will simply neglect these effects.

Throughout the following derivations, we will need to describe the gravitational potential associated with relief along a density interface at mean radius r_i . For this, we will make use of the equations

$$U(\mathbf{r}) = \begin{cases} \frac{GM}{r} \sum_{l=0}^{\infty} \sum_{m=-l}^l \left(\frac{r_i}{r}\right)^l C_{lm}^{(i)+} Y_{lm}(\theta, \phi) & \text{for } r \geq r_i \\ \frac{GM}{r} \sum_{l=0}^{\infty} \sum_{m=-l}^l \left(\frac{r}{r_i}\right)^{l+1} C_{lm}^{(i)-} Y_{lm}(\theta, \phi) & \text{for } r < r_i, \end{cases} \quad (5)$$

where $C_{lm}^{(i)}$ represents the spherical harmonic coefficients of the gravitational potential at a reference radius r_i , G is the gravitational constant, and M is the total mass of the body. The superscripts $+$ and $-$ associated with the potential coefficients are for the cases where the potential is evaluated above and below the interface, respectively. To first order in h_{lm} , we have (e.g., Wieczorek, 2015)

$$C_{lm}^{(i)} = \frac{4\pi \Delta\rho_i r_i^2 h_{lm}^{(i)}}{M(2l+1)}, \quad (6)$$

with C_{lm}^+ and C_{lm}^- being equal. Only later when calculating the gravitational attraction of the surface relief will higher-order terms be considered.

When evaluating the potential along a density interface, it will be necessary to evaluate the radius of the relief of this surface raised to the n th power in terms of spherical harmonics. Starting with equation (3), the first-order Taylor expansion of this quantity with respect to the (small) nonspherical shape is

$$[r^{(i)}(\theta, \phi)]^n = r_i^n \left(1 + \sum_{l=1}^{\infty} \sum_{m=-l}^l \frac{h_{lm}^{(i)}}{r_i} Y_{lm} \right)^n \simeq r_i^n \left(1 + n \sum_{l=1}^{\infty} \sum_{m=-l}^l \frac{h_{lm}^{(i)}}{r_i} Y_{lm} \right). \quad (7)$$

In the subsequent derivations, all terms involving products of $h_{lm} h_{l'm'}$ will be neglected, given their small magnitudes. As a result of this, there will be no coupling between terms involving two different spherical harmonic degrees or two different angular orders, and it will be possible to resolve the system of linear equations separately for each degree and order. Thus, when analyzing a single degree l and order m , the above equation can be reduced to

$$[r^{(i)}(\theta, \phi)]^n \simeq r_i^n \left(1 + n \frac{h_{lm}^{(i)}}{r_i} Y_{lm} \right). \quad (8)$$

Though this study uses a first-order approach when calculating the relief along hydrostatic interfaces, it will be shown later that the influence of the nonhydrostatic component of the gravity field is considerably larger than the differences between first-order and higher-order formulations.

In the following subsections, we derive expressions for each of the terms in equation (1) along the interfaces that are assumed to be in hydrostatic equilibrium. Then we impose the condition of hydrostatic equilibrium by requiring the potential along each of these interfaces to be constant.

2.1.1. U_0^+ and U_0^-

We start by considering an unperturbed reference state that corresponds to a spherically symmetric mass distribution. The potential will be computed on an arbitrary nonspherical surface i , considering the gravitational potential that arises from mass both above, $U_0^{(i)-}$, and below the surface, $U_0^{(i)+}$. The gravitational potential at radius r resulting from the mass beneath the observation point is simply

$$U_0^+(r) = \frac{GM(r)}{r}, \quad (9)$$

where $M(r)$ is the total mass beneath radius r . The total mass beneath radius r , where r is closest to and larger than r_i , is

$$M(r) = \sum_{j=1}^i \frac{4\pi\rho_{j-1}}{3} (r_j^3 - r_{j-1}^3) + \frac{4\pi\rho_i}{3} (r^3 - r_i^3). \quad (10)$$

Using the first-order approximation of $1/r$ and r^3 from equation (8), the potential on the interface is

$$U_0^{(i)+} = \frac{G}{r_i} \left(1 - \frac{h_{lm}^{(i)}}{r_i} Y_{lm} \right) \left[M(r_i) + \frac{4\pi\rho_i}{3} \left\{ r_i^3 \left(1 + 3 \frac{h_{lm}^{(i)}}{r_i} Y_{lm} \right) - r_i^3 \right\} \right]. \quad (11)$$

We are interested only in that part of the potential that varies along the interface. Keeping only those terms that depend on Y_{lm} and that are also linear in h_{lm} yields

$$U_{lm,0}^{(i)+} = -GM(r_i) \frac{h_{lm}^{(i)}}{r_i^2} + 4\pi G\rho_i r_i h_{lm}^{(i)}. \quad (12)$$

Next consider the gravitational potential from mass above the observation point with respect to the 1-dimensional reference state. The potential of a constant density finite-thickness spherical shell defined by radii r_1 and r_2 is shown easily to be (e.g., Blakely, 1995)

$$U_0^- = 2\pi G\rho_i (r_2^2 - r_1^2), \quad (13)$$

where ρ_i is the density of the shell. Summing from r to the surface r_N gives

$$U_0^{(i)-} = \sum_{j=i+1}^{N-1} 2\pi G\rho_j (r_{j+1}^2 - r_j^2) + 2\pi G\rho_i (r_{i+1}^2 - r^2). \quad (14)$$

Using the definition of r for a single harmonic Y_{lm} and retaining only those terms that depend upon this harmonic yields

$$U_{lm,0}^{(i)-} = -4\pi G\rho_i r_i h_{lm}^{(i)}. \quad (15)$$

Combining the potential from mass above and below the observation point yields

$$U_{lm,0}^{(i)+} + U_{lm,0}^{(i)-} = -GM(r_i) \frac{h_{lm}^{(i)}}{r_i^2}. \quad (16)$$

2.1.2. U^+ and U^-

Next consider the gravitational potential from the nonspherically symmetric mass distributions related to relief along all hydrostatic interfaces below and including interface i , where $i \leq L$. The potential at radius r for a single harmonic is given by

$$U^+(\mathbf{r}) = \sum_{j=1}^i \frac{GM}{r} \left(\frac{r_j}{r}\right)^l \frac{4\pi \Delta\rho_j r_j^2 h_{lm}^{(j)}}{M(2l+1)} Y_{lm}, \quad (17)$$

where $r \geq r_i$. Since these terms are linear in h_{lm} , when evaluating the potential along interface i , we can simply make the substitution

$$[r^{(i)}(\theta, \phi)]^l = [r_i + h_{lm}^{(i)} Y_{lm}(\theta, \phi)]^l \simeq r_i^l, \quad (18)$$

which yields

$$U_{lm}^{(i)+} = \sum_{j=1}^i \frac{4\pi G \Delta\rho_j}{(2l+1)} \left(\frac{r_j^{l+2}}{r_i^{l+1}}\right) h_{lm}^{(j)}. \quad (19)$$

Next consider the gravitational potential from relief along all hydrostatic interfaces above i and below $L+1$. The potential at radius r for a single harmonic is given by

$$U^-(\mathbf{r}) = \sum_{j=i+1}^L \frac{GM}{r} \left(\frac{r}{r_j}\right)^{l+1} \frac{4\pi \Delta\rho_j r_j^2 h_{lm}^{(j)}}{M(2l+1)} Y_{lm}, \quad (20)$$

where $r < r_i$. When evaluating the potential along interface i , we make the same substitution as above and arrive at

$$U_{lm}^{(i)-} = \sum_{j=i+1}^L \frac{4\pi G \Delta\rho_j}{(2l+1)} \left(\frac{r_i^l}{r_j^{l-1}}\right) h_{lm}^{(j)}. \quad (21)$$

2.1.3. U_{rot}

For a reference frame fixed to a rotating body, the pseudo-rotational potential can be expressed as (e.g., Wieczorek, 2015)

$$U_{\text{rot}} = \frac{\omega^2 r^2 \sin^2 \theta}{2} = \omega^2 r^2 \left(\frac{1}{3} Y_{00} - \frac{1}{3\sqrt{5}} Y_{20} \right). \quad (22)$$

Using the first-order approximation of equation (8) for r along interface i yields

$$U_{\text{rot}}^{(i)} = \frac{\omega^2 r_i^2}{3} - \frac{\omega^2 r_i^2}{3\sqrt{5}} Y_{20}. \quad (23)$$

Finally, the component of the rotational potential to spherical harmonic degree l and m is

$$U_{lm,\text{rot}}^{(i)} = -\frac{\omega^2 r_i^2}{3\sqrt{5}} \delta_{l2} \delta_{m0}, \quad (24)$$

where δ is the Kronecker delta function. In this equation, we have ignored terms that are proportional to $\omega^2 r_i h_{lm}^{(i)}$, which are considerably smaller than those proportional to $\omega^2 r_i^2$. These are typically ignored in treatments of hydrostatic equilibrium that are first order in the expansion parameter $q = \omega^2 R/g$, where g is the mean gravitational acceleration at the surface of radius R . Regardless, as will be shown in sections 2.3 and 3, given that the degree-2 terms of the relief h_{lm} are often significantly larger than those of the other degrees, inclusion of this term can make a small improvement to the degree-2 hydrostatic solution.

2.1.4. U_{lith}

The last contribution to the gravitational potential along a hydrostatic interface comes from mass anomalies in the lithosphere. In practice, the lithosphere of a body encompasses both the crust and uppermost portion of the mantle. The gravitational component from the lithosphere will be considered as arising from two sources: the observed surface relief of the body and a mass sheet at an arbitrary depth, here taken to be the crust-mantle interface. The gravitational attraction associated with the surface relief is by far the largest contributor of the two, and the mass sheet accounts for all remaining unmodeled contributions, such as might be due to lateral variations in crustal thickness, porosity, composition, and temperature. Though the mass sheet term could be modeled explicitly under certain simplifying assumptions (such as using constant density layers and/or elastic flexure), the approach chosen here is to lump all these effects into a single term at a prescribed depth and to interpret the origin of this term afterward. It will be shown later that the depth utilized for this effective source layer has only a modest influence on our results.

Given that the gravitational attraction of the surface relief is large (in part because of the high-density contrast), we will model this contribution using the higher-order approach of Wicczorek and Phillips (1998). In particular, the spherical harmonic coefficients for use in equation (5) are given by

$$C_{lm}^{(N)+} = \frac{4\pi \Delta\rho_N r_N^3}{M(2l+1)} \sum_{n=1}^{l+3} \frac{{}^n h_{lm}^{(N)}}{r_N^n n!} \frac{\prod_{j=1}^n (l+4-j)}{(l+3)}, \quad (25)$$

$$C_{lm}^{(N)-} = \frac{4\pi \Delta\rho_N r_N^3}{M(2l+1)} \sum_{n=1}^{\infty} \frac{{}^n h_{lm}^{(N)}}{r_N^n n!} \frac{\prod_{j=1}^n (l+j-3)}{(l-2)}, \quad (26)$$

where the term ${}^n h_{lm}$ is defined to be the spherical harmonic coefficients of the function $h^n(\theta, \phi)$. Using the same approximation as in the preceding subsections, the contribution of the surface relief to the potential along hydrostatic interfaces is given by

$$U_{lm,\text{lith}}^{(i)} = GM \left(\frac{r_i^l}{r_N^{l+1}} \right) C_{lm}^{(N)-}. \quad (27)$$

The remainder of the contribution to the lithospheric potential is modeled as arising from a mass sheet at average radius r_{N-1} , which is given by

$$U_{lm,\text{lith}}^{(i)} = \frac{4\pi G}{(2l+1)} \left(\frac{r_i^l}{r_{N-1}^{l-1}} \right) \sigma_{lm}^{(N-1)}. \quad (28)$$

In practice, σ_{lm} will be determined by requiring that the total gravitational potential of the body is equal to the observed potential.

2.2. Hydrostatic Equilibrium

The condition of hydrostatic equilibrium requires that the gravitational potential be constant along interfaces of constant density. Thus, after summing all components of the gravitational potential, those components along a density interface that depend upon degree l and order m must be identically zero. Using the equations from the previous sections for all interfaces $i \leq L$, this translates to

$$0 = -GM(r_i) \frac{h_{lm}^{(i)}}{r_i^2} + \sum_{j=1}^i \frac{4\pi G \Delta\rho_j}{(2l+1)} \left(\frac{r_j^{l+2}}{r_i^{l+1}} \right) h_{lm}^{(j)} + \sum_{j=i+1}^L \frac{4\pi G \Delta\rho_j}{(2l+1)} \left(\frac{r_i^l}{r_j^{l-1}} \right) h_{lm}^{(j)} - \frac{\omega^2 r_i^2}{3\sqrt{5}} \delta_{l2} \delta_{m0} + \frac{4\pi G}{(2l+1)} \left(\frac{r_i^l}{r_{N-1}^{l-1}} \right) \sigma_{lm}^{(N-1)} + GM \left(\frac{r_i^l}{r_N^{l+1}} \right) C_{lm}^{(N)-}. \quad (29)$$

In addition to this condition, the potential resulting from all interfaces must be equal to the observed value:

$$\frac{GM}{R_0} C_{lm}^{\text{obs}} = \sum_{j=1}^L \frac{4\pi G \Delta\rho_j}{(2l+1)} \left(\frac{r_j^{l+2}}{R_0^{l+1}} \right) h_{lm}^{(j)} + \frac{4\pi G}{(2l+1)} \left(\frac{r_{N-1}^{l+2}}{R_0^{l+1}} \right) \sigma_{lm}^{(N-1)} + GM \left(\frac{r_N^l}{R_0^{l+1}} \right) C_{lm}^{(N)+}, \quad (30)$$

where the observed coefficients are referenced to the radius R_0 . Equations (29) and (30) can be written in matrix notation for each spherical harmonic of degree l and order m as

$$\mathbf{A}\mathbf{h} = \mathbf{b}. \quad (31)$$

Here \mathbf{h} is a vector containing the spherical harmonic coefficients of the lithospheric mass sheet and the relief at each interface i (excluding $i = 0$)

$$h_i = \begin{cases} h_{lm}^{(i)} & \text{for } 1 \leq i \leq L \\ \sigma_{lm}^{(N-1)} & \text{for } i = N-1, \end{cases} \quad (32)$$

and the matrix \mathbf{A} depends upon the density profile and location of the density interfaces as given by

$$\begin{aligned} A_{ij} &= \frac{4\pi G \Delta\rho_j}{(2l+1)} \left(\frac{r_j^{l+2}}{r_i^{l+1}} \right) && \text{for } j < i \leq L \\ &= -\frac{GM(r_i)}{r_i^2} + \frac{4\pi G \Delta\rho_i r_i}{(2l+1)} && \text{for } i = j \leq L \\ &= \frac{4\pi G \Delta\rho_j}{(2l+1)} \left(\frac{r_i^l}{r_j^{l-1}} \right) && \text{for } i < j \leq L \\ &= \frac{4\pi G}{(2l+1)} \left(\frac{r_i^l}{r_{N-1}^{l-1}} \right) && \text{for } j = N-1, i \leq L \\ &= \frac{4\pi G \Delta\rho_j}{(2l+1)} \left(\frac{r_j^{l+2}}{R_0^{l+1}} \right) && \text{for } i = N-1, j \leq L \\ &= \frac{4\pi G}{(2l+1)} \left(\frac{r_{N-1}^{l+2}}{R_0^{l+1}} \right) && \text{for } i = j = N-1. \end{aligned} \quad (33)$$

The vector \mathbf{b} contains that part of the rotational contribution that does not depend upon h_{lm} , as well as the observed gravitational potential coefficient and gravitational potential of the surface relief:

$$b_i = \begin{cases} \frac{\omega^2 r_i^2}{3\sqrt{5}} \delta_{l2} \delta_{m0} - GM \left(\frac{r_i^l}{r_N^{l+1}} \right) C_{lm}^{(N)-} & \text{for } i \leq L \\ \frac{GM}{R_0} C_{lm}^{\text{obs}} - GM \left(\frac{r_N^l}{R_0^{l+1}} \right) C_{lm}^{(N)+} & \text{for } i = N-1. \end{cases} \quad (34)$$

With \mathbf{A} and \mathbf{b} computed, equation (31) can be solved individually for each spherical harmonic degree and order.

2.3. Corrections to the Degree-2 and Degree-4 Terms

In the treatment of the hydrostatic equilibrium of a planet, the zonal degree-2 surface relief is usually considerably larger than the other degrees and orders. In this section, we will consider an additional small term in the rotational potential of equation (23) that will be shown later to improve the accuracy of both the zonal degree-2 and degree-4 solutions for fluid planets.

When expanding equation (22) using the first-order approximation of equation (8), it can be shown that there are additional small terms to the rotation potential, δU , that were previously ignored in equation (23):

$$\delta U_{\text{rot}}^{(i)} = \frac{2\omega^2 r_i h_{lm}^{(i)} Y_{lm}}{3} - \frac{2\omega^2 r_i h_{lm}^{(i)} Y_{lm} Y_{20}}{3\sqrt{5}}. \quad (35)$$

Though this contribution to the rotational potential is smaller than that of equation (23) by a factor proportional to $h_{lm}^{(i)}/r_i$, this could be nonnegligible for planets with many kilometers of rotational flattening. The last term of the above equation involves the product of two spherical harmonic functions, and this itself can be reexpressed as a weighted sum of spherical harmonic functions up to a maximum degree $l + 2$. In particular, by defining the function p as the product $Y_{20} Y_{lm}$, we have

$$p = (Y_{lm} Y_{20}) = \sum_{l'=0}^{l+2} \sum_{m'=-l'}^{l'} p_{l'm'}(20; lm) Y_{l'm'}, \quad (36)$$

where the coefficients $p_{l'm'}(20; lm)$ are given by

$$p_{l'm'}(20; lm) = \frac{1}{4\pi} \int_{\Omega} (Y_{lm} Y_{20}) Y_{l'm'} d\Omega. \quad (37)$$

These coefficients can be calculated easily using numerical spherical harmonic expansion techniques (or alternatively, using Clebsch-Gordan coefficients).

In order to obtain a linear solution that does not involve coupling between different degrees and orders, we retain only that component of p from equation (37) that has the same spherical harmonic degree and order as h_{lm} . Under this assumption, the additional contribution to the rotational potential for spherical harmonic degree l and order m reduces to

$$\delta U_{lm,rot}^{(i)} = \frac{2\omega^2 r_i h_{lm}^{(i)}}{3} \left(1 - \frac{p_{lm}(20; lm)}{\sqrt{5}} \right). \quad (38)$$

It is straightforward to show that the inclusion of this term modifies only the diagonal elements of the matrix A in section 2.2 by the addition of

$$\delta A_{ii} = \frac{2\omega^2 r_i}{3} \left(1 - \frac{p_{lm}(20; lm)}{\sqrt{5}} \right) \quad \text{for } i \leq L. \quad (39)$$

Though this small contribution to the rotational potential could be computed for any degree and order, in practice, we will make use only of the zonal degree-2 correction. This term is not included in treatments of hydrostatic equilibrium that are first order in the expansion parameter $q = \omega^2 R/g$, and its utility will be assessed in section 3.

As seen in equations (35)–(37), relief h_{lm} along an interface will generate a small contribution to the rotational potential at degrees other than just degree l . In general, the h_{20} term of a body will be by far the largest as a result of the rotational flattening, and the additional contributions to the rotational potential will thus be the largest for those components that depend upon h_{20} . We will assume that the degree-2 relief of all interfaces has been determined previously by solving the equations of the preceding section. Then, using these terms, a correction will be computed that is applicable when computing the degree-4 relief.

Using the definition of $p_{l'm'}(20; lm)$ in equation (37), the last term of equation (23) for $l = 2$ can be expanded as

$$-\frac{2\omega^2 r_i h_{2m}^{(i)}}{3\sqrt{5}} Y_{2m} Y_{20} = -\frac{2\omega^2 r_i h_{2m}^{(i)}}{3\sqrt{5}} \sum_{l'=0}^4 \sum_{m'=-l'}^{l'} p_{l'm'}(20; 2m) Y_{l'm'}. \quad (40)$$

Using the properties of the Clebsch-Gordan coefficients, it can be shown that $p_{l'm'}(20; 2m)$ is nonzero only when l' is 0, 2, and 4 and when $m' = m$. In the previous derivations of this section, only the $l' = 2$ term was considered. The degree-4 term of equation (40) could be important given the large amplitude of the h_{2m} relief, and these terms should be included in equation (29) when solving for the degree-4 relief. Given that the components of the above equation do not depend upon h_{4m} , it is straightforward to show that it is only necessary to add the correction

$$\delta b_i = \frac{2\omega^2 r_i h_{2m}^{(i)}}{3\sqrt{5}} p_{4m}(20; 2m) \quad \text{for } l = 4, |m| \leq 2, i \leq L, \quad (41)$$

to the vector \mathbf{b} in equation (34). Though this contribution could be computed for all angular orders of degree 4, in practice, we will make use only of the zonal term, which is proportional to the zonal degree-2 term.

2.4. Tidal Potentials

For a reference frame fixed to a satellite that is in synchronous rotation about a central planet, the static part of the tidal potential can be written as (e.g., Wicczorek, 2015)

$$U^{\text{tide}} \simeq \frac{GM_p r^2}{a^3} \left(-\frac{\sqrt{5}}{10} Y_{20} + \frac{1}{4} \sqrt{\frac{12}{5}} Y_{22} \right), \quad (42)$$

where M_p is the mass of the planet and a is the semimajor axis of the satellite. Using the first-order approximation for r^2 , the potential on each interface i is

$$U_{\text{tide}}^{(i)} = \left(\frac{GM_p r_i^2}{a^3} \right) \left(-\frac{\sqrt{5}}{10} Y_{20} + \frac{1}{4} \sqrt{\frac{12}{5}} Y_{22} \right) + \left(\frac{GM_p r_i^2}{a^3} \right) \left(-\frac{\sqrt{5}}{5} \frac{h_{lm}^{(i)}}{r_i} Y_{lm} Y_{20} + \frac{1}{2} \sqrt{\frac{12}{5}} \frac{h_{lm}^{(i)}}{r_i} Y_{lm} Y_{22} \right). \quad (43)$$

Following the same approach as in section 2.3, the products of two spherical harmonics are expanded in spherical harmonics, and only those terms that depend on Y_{lm} are retained. The spherical harmonic coefficients of the potential along interface i can thus be given by

$$U_{lm,\text{tide}}^{(i)} = \left(\frac{GM_p r_i^2}{a^3} \right) \left(-\frac{\sqrt{5}}{10} \delta_{l2} \delta_{m0} + \frac{1}{4} \sqrt{\frac{12}{5}} \delta_{l2} \delta_{m2} \right) + h_{lm}^{(i)} \left(\frac{GM_p r_i}{a^3} \right) \left(-\frac{\sqrt{5}}{5} p_{lm}(20; lm) + \frac{1}{2} \sqrt{\frac{12}{5}} p_{lm}(22; lm) \right). \quad (44)$$

It is trivial to modify the elements of the matrix equation (equation (31)) to account for the tidal potential. For the elements of \mathbf{A} in equation (33), it is only necessary to modify the diagonal terms

$$A_{ii} = -\frac{GM(r_i)}{r_i^2} + \frac{4\pi G \Delta \rho_i r_i}{(2l+1)} + \frac{2\omega^2 r_i}{3} \left(1 - \frac{p_{lm}(20; lm)}{\sqrt{5}} \right) + \left(\frac{GM_p r_i}{a^3} \right) \left(-\frac{\sqrt{5}}{5} p_{lm}(20; lm) + \frac{1}{2} \sqrt{\frac{12}{5}} p_{lm}(22; lm) \right) \quad \text{for } i \leq L, \quad (45)$$

and for the vector \mathbf{b} , the elements are given by the modification

$$b_i = \begin{cases} \frac{\omega^2 r_i^2}{3\sqrt{5}} \delta_{l2} \delta_{m0} + \frac{GM_p r_i^2}{a^3} \left(\frac{\sqrt{5}}{10} \delta_{l2} \delta_{m0} - \frac{1}{4} \sqrt{\frac{12}{5}} \delta_{l2} \delta_{m2} \right) - GM \left(\frac{r_i}{R_N} \right) C_{lm}^{(N)-} & \text{for } i \leq L \\ \frac{GM}{R_0} C_{lm}^{\text{obs}} - GM \left(\frac{r_i}{R_0^{l+1}} \right) C_{lm}^{(N)+} & \text{for } i = N - 1. \end{cases} \quad (46)$$

It is noted that the term GM_p/a^3 is approximately equal to ω^2 when the mass of the satellite is small in comparison to that of the planet it orbits.

The largest contributions to the shape of a tidally deformed synchronous satellite are generally the terms h_{20} and h_{22} . Similar to the discussion in section (2.3), these terms could generate small contributions of spherical harmonic degree-4 to the tidal potential. Accounting for these contributions, however, is somewhat more complicated than for the case of the rotational potential, as several of the spherical harmonic degrees and order become coupled. In particular, when considering the relief h_{20} and h_{22} terms, additional terms to the potential would be generated that are proportional to $h_{20} Y_{22}$, $h_{20} Y_{42}$, $h_{22} Y_{20}$, $h_{22} Y_{40}$, and $h_{22} Y_{44}$. These terms will be ignored in this study as they have a small amplitude. Though they are certainly negligible for Earth's Moon (which will be investigated in section 4.4), they could be of importance for application to other satellites, such as Jupiter's moon Io.

Table 1
Observed h_{20} and h_{40} for the Surface of Mars and Predicted Values Assuming Hydrostatic Equilibrium

h_{20} (m)	h_{40} (m)	Source
-5,966.2	224.7	Observed (MarsTopo2600, Wieczorek, 2015)
-5030.4	—	First order (using code of Chambat et al., 2010)
-5,049.3	10.4	Second order (using code of Chambat et al., 2010)
-5,053.9	8.3	This study
-5,030.0	8.2	This study, ignoring equation (39)

3. Validation

The accuracy of the above formalism will be tested against known entirely fluid solutions for Mars and Ceres. We first compute the relief along all interfaces assuming that the bodies are entirely hydrostatic. Then, we compare these solutions with those obtained using the second-order theory of Chambat et al. (2010), which is itself based on Kopal (1960) and Lanzano (1982). Finally, we demonstrate that the surface of Mars is in fact far from hydrostatic equilibrium.

For our model illustrated in Figure 1, when a body has no lithosphere, the radial index corresponding to the index L is equivalent to the index N of the surface. To obtain a purely hydrostatic solution, it is only necessary to make use of the $L \times L$ submatrix of \mathbf{A} in equation (31). In particular, the last row and column of \mathbf{A} and \mathbf{b} , which contain the lithospheric terms and known gravity field, are simply discarded. The resulting equations are equivalent to a first-order discretized version of Clairaut's integral equation (see equation 12, p. 185, Jeffreys, 1970), with the exception of the inclusion of the small term proportional to $\omega^2 h_{lm}$ as described in section 2.3. The equations in Chambat et al. (2010) contain terms of order h_{lm}^2 and require the solution of a second-order differential equation.

For our first test, we make use of a density profile of Mars that is derived from the Mars bulk-silicate compositional model of Taylor (2013). This model (TAAK, see Table 4) has a core radius of 1,791 km and is taken from the Mars reference models presented in Smrekar et al. (2019). The predicted hydrostatic flattening corresponds to a difference of 17 km between the poles and equator, and the observed values of h_{20} and h_{40} , our predicted values, and those predicted by the first- and second-order hydrostatic theories from the numerical code of Chambat et al. (2010) are given in Table 1.

Somewhat remarkably, our first-order results and the second-order results using the code of Chambat et al. (2010) for the zonal degree-2 surface shape h_{20} are found to differ by only 0.09%. If we were to have ignored the small term of equation (39), our results would be nearly identical to the first-order value from the same code. Our first-order theory provides a value for the zonal degree-4 shape h_{40} that is comparable to the second-order prediction but differs by 21%.

For Mars, it should be emphasized that the observed shape deviates substantially from the predicted hydrostatic values. For the zonal degree-2 term, the difference is about 15%, whereas for the zonal degree-4 term,

Table 2
Observed ($a - c$) for Ceres and Predicted Values for a Uniform Density Body Assuming Hydrostatic Equilibrium

$a - c$ (km)	Source
37.2 ± 0.1	Observed (Park et al., 2016)
37.908	First order (Rambaux et al., 2015)
39.561	Second order (Rambaux et al., 2015)
39.739	Third order (Rambaux et al., 2015)
39.764	Exact Maclaurin ellipsoid (Rambaux et al., 2015)
40.431	This study
41.019	$l = 2$, this study
37.909	$l = 2$, this study, ignoring equation (39)

the two differ by a factor of 21. It is thus clear that the nonhydrostatic contribution to the shape of Mars exceeds greatly the small differences between the first- and second-order theories. It is thus not necessary to apply a higher-order hydrostatic theory to a planet like Mars that is far from hydrostatic equilibrium.

For Ceres, we test our approach using the constant density model that was tested in Rambaux et al. (2015). Though more realistic density profiles resulting from internal differentiation were also tested in that study, the homogeneous case was found to give the largest discrepancies between the first- and third-order theories of figures. The constant density model is not meant to provide the best fit to the observations and is used here only as a numerical test. In Table 2, we provide the difference in the equatorial and polar axes, $a - c$, predicted for hydrostatic equilibrium, as well as the measured value of Park et al. (2016). A difference of 1.86 km was found between the exact solution of a Maclaurin ellipsoid and their first-order solution, which corresponds to a relative error of 4.7%.

Using our approach, we find a difference of only 0.67 km for $a - c$ with that predicted for a Maclaurin ellipsoid, which corresponds to a relative error of 1.7%. The better concordance is a result of us having calculated a degree-4 term and having included the correction of equation (39), both of which are generally neglected in first-order theories. If we were to have neglected the degree-4 term, the difference with respect to the exact solution would have increased to 1.26 km (3.2%). If we were to have also neglected the correction of equation (39), our solution would be nearly identical to the first-order solution of Rambaux et al. (2015). Thus, though a higher-order approach may be necessary to model the hydrostatic shape of Ceres for certain applications, for this particular model, our approach provides a value that is more accurate by almost a factor of three in comparison to previous first-order techniques.

4. Applications

The theory developed in section 2 can be applied to any terrestrial planet, dwarf planet, or differentiated asteroid or moon whose gravity field is known. Here we demonstrate several potential applications to Mars and Earth's Moon. First, we calculate the shape of hydrostatic interfaces in Mars, which are shown to be perturbed by the gravitational potential associated with the Tharsis province. Second, we compute the gravitational potential of these interfaces and invert the remaining lithospheric signal for crustal thickness variations. Third, using our computed shape of the core-mantle boundary, we determine how the lithospheric gravity affects the free core nutation frequency. Finally, we compute the shape of the core-mantle boundary of the Moon, which is important for interpretations of LLR data.

4.1. Mars: Shape of Hydrostatic Interfaces

In calculating the shape of hydrostatic interfaces in the planet Mars, we will make use of the 120 degree and order gravity field GMM-3 of Genova et al. (2016) and the spherical harmonic shape model of Wieczorek (2015), both truncated at degree 90. For the density profile of the planet, we will make use of the model TAAK from Smrekar et al. (2019) that is based on the bulk-silicate compositional model of Taylor (2013) and which has a core radius of 1,791 km (see also Table 4). Only the density profile of this model beneath the maximum depth of the lithosphere is required for our calculations, given that the gravity contribution of the lithosphere is treated separately (see Figure 1). When calculating the gravitational contribution of the surface topography, a crustal density of 2,900 kg/m³ will be assumed. A large part of the remainder of the nonhydrostatic mass anomalies in the lithosphere is likely a result of relief along the crust-mantle interface, so we will assume a depth to this interface of 45 km, which is close to the predicted average thickness of the crust (e.g., Neumann et al., 2004; Wieczorek & Zuber, 2004). Though it is likely that a small portion of the lithospheric signal could come from shallower portions of the crust (such as from magmatic intrusions or lateral variations in crustal composition), it is unlikely that significant density anomalies would be present in the lithospheric mantle beneath the crust.

The geoid of Mars (i.e., the shape of an equipotential surface) is plotted in the top row of Figure 2 using the GMM-3 gravity model. In the left column, the heights are referenced to the mean radius of the planet, whereas in the right column, the heights are referenced to the shape predicted if the planet was entirely fluid. In all images, the central meridian is 100° W, which corresponds to the mean longitude of the Tharsis volcanic province. A difference in elevation of about 17 km is visible from pole to equator, which is primarily a result of the rotational flattening of the planet. Nevertheless, as is evident in the right column, there are about 3 km of relief superposed on that predicted for a purely fluid planet. These geoid anomalies are primarily a result of the volcanic load of the Tharsis province, several large volcanoes that are superposed on

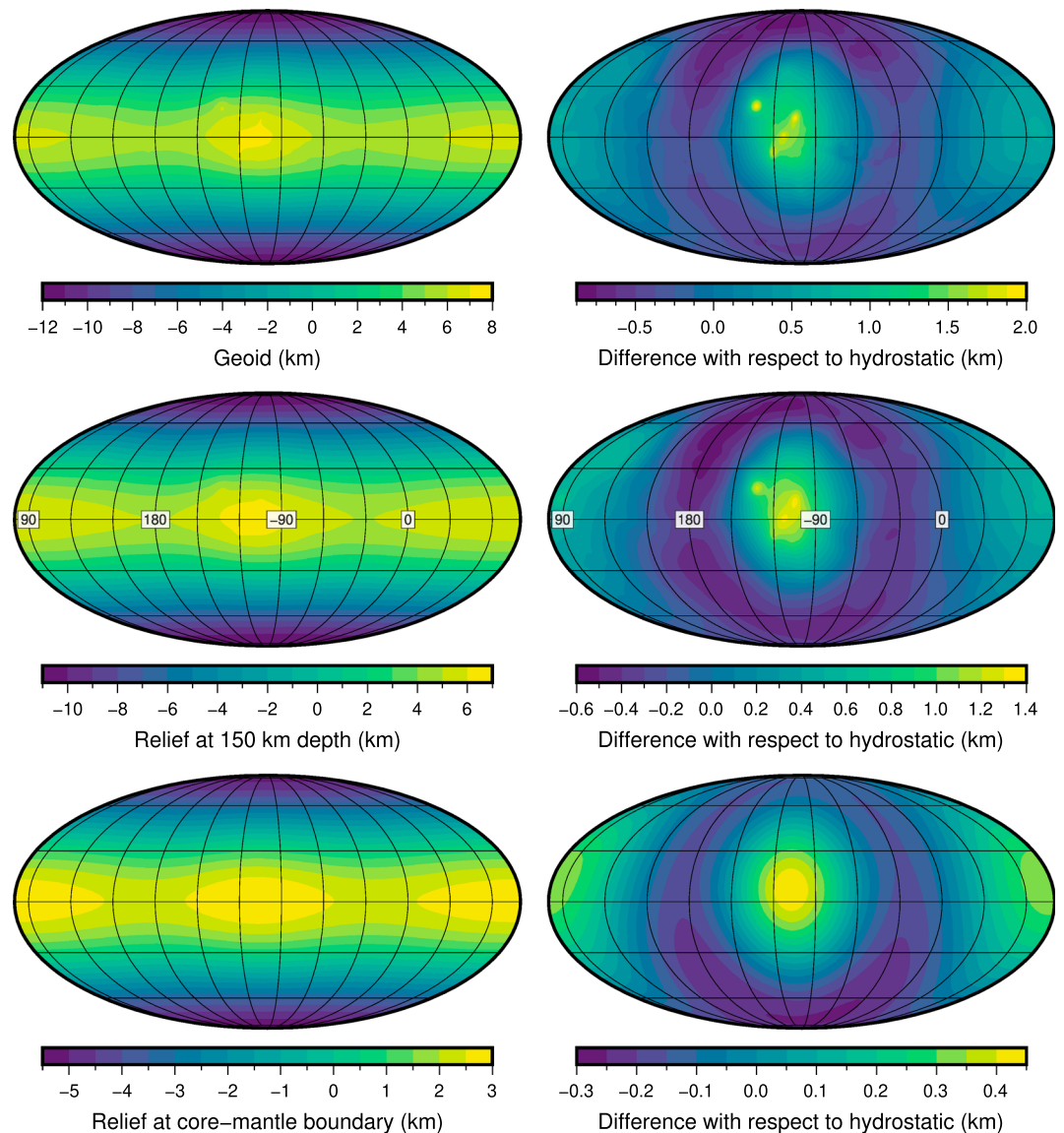


Figure 2. The geoid of Mars, hydrostatic relief along an interface at 150-km depth, and hydrostatic relief of the core-mantle boundary. Mass anomalies within the lithosphere were placed at a depth of 45 km, the maximum thickness of the lithosphere was assumed to be 150 km, and the core radius is 1,791 km. The relief is calculated with respect to the mean radius of each interface in the left panel, whereas in the right panel, the relief is calculated with respect to the shape expected for an entirely fluid planet. Images are in a Mollweide projection with a central meridian of 100° W longitude, which corresponds to the center of the Tharsis province. The color bars for each image are scaled to the minimum and maximum values of the data.

this province (such as Olympus Mons), and the flexural response of the planet to these loads (e.g., Phillips, Zuber, Solomon, et al., 2001). For comparison, the 3 km of geoid relief on Mars is considerably larger than the few hundred meters of relief of Earth's geoid (e.g., Wiczorek, 2015).

The predicted hydrostatic relief at 150-km depth is plotted in the middle row of Figure 2. For this calculation, we assumed a maximum lithospheric thickness of 150 km, which corresponds approximately to the best-fitting elastic thickness of 140 km that was determined beneath the South polar cap using gravity and topography data (Wiczorek, 2008). Nevertheless, we note that this value is shallower than the inferred elastic thickness of more than 300 km beneath the North polar cap that is based on radar data (Phillips, Zuber, Smrekar, et al., 2001). The interface at 150-km depth is close to the mass anomalies located at the surface and at 45-km depth, and the computed hydrostatic relief along this interface is found to vary by 2 km (when referenced to that predicted for an entirely fluid planet). This relief is comparable to the 3 km of relief of

Table 3
Low-Degree Spherical Harmonic Coefficients (in Meters) of the Relief Along the Core-Mantle Interface of Mars for Interior Model TAAK

l	m	h_{lm}	$h_{l,-m}$
0	0	1,791,372.60	
1	0	45.53	
1	1	3.26	25.58
2	0	-2,361.32	
2	1	-2.95	-1.62
2	2	-121.40	68.06
3	0	-10.67	
3	1	4.34	20.89
3	2	-10.86	4.43
3	3	24.95	15.13

Note. For an entirely fluid planet, all terms would be zero except h_{20} , which is predicted to be $-2,276.36$.

the geoid, and the two maps differ only somewhat as a result of the attenuation of the shortest wavelength signals.

The hydrostatic relief at the core-mantle boundary is shown in the bottom row of Figure 2, and the spherical-harmonic coefficients of the core shape are given in Table 3. The largest signal is a zonal component that has a difference in radius between the poles and equator of about 8 km. At this depth, the gravitational potential from the lithosphere is highly attenuated, and the high-frequency structure associated with the interior of the Tharsis province in the previous images is largely absent. Regardless, as is shown in the right column, even at these depths, there is still about 710 m of relief along the core-mantle boundary with respect to that associated for an entirely fluid planet. This relief is almost entirely the result of the degree-2 terms of the lithospheric gravity field. The amplitude of individual degree-4 terms is less than 5 m.

We note that the shape of the core of Mars is predicted to have a small degree-1 component. In the above model, this corresponds to an amplitude of 87 m and implies that the core is offset from the center-of-mass of the planet by the same amount. This may at first seem counterintuitive but is easy to explain by use of a simple model. Consider a planet that contains two separate degree-1 mass anomalies at radii r_1 and r_2 with respective spherical-harmonic coefficients $C_{1m}^{(1)}$ and $C_{1m}^{(2)}$. To be in center-of-mass coordinates, the combined gravitational contribution of the two is required to be exactly zero exterior to the planet, and this implies that $C_{1m}^{(1)} = -C_{1m}^{(2)}(r_2/r_1)$. However, if one were to calculate the gravitational potential below these two interfaces, one would find that the degree-1 potential would be nonzero. In fact, the degree-1 potential would be zero everywhere only if the radii of the two interfaces coincided. Using a similar argument, it is easy to show that the principal moments of inertia of the core are not required to be aligned with those of the entire body. In fact, for the TAAK model, we find that the maximum principal moment of the core is inclined by 0.05° with respect to the mean rotation axis of the planet.

Lastly, we quantify how our results depend upon the assumed crustal density and depth of the lithospheric mass anomalies. Varying the density of the crust from 2,500 to 3,300 kg/m³ is found to have only a small effect, with the relief at 150-km depth and the core-mantle interface changing by no more than about 78 m. Modifying the depth of the mass anomalies in the lithosphere, however, has a slightly more important effect. Our nominal case employed a depth of 45 km, which corresponds approximately to the base of the crust, and as extreme end-members, we varied this depth from the surface to 100 km. For the hydrostatic relief at 150-km depth, this caused variations up to 310 m, which corresponds to about 10% of the maximum relief along this interface when referenced to the entirely fluid solution. For the core-mantle boundary, the maximum difference was found to be 143 m, which is about 32% of the maximum relief along this interface when referenced to the entirely fluid solution.

4.2. Mars: Global Crustal Thickness

The main contributions to the observed gravity field of Mars come from the shape of the surface, variations in thickness of the crust, and the hydrostatic flattening of density interfaces in the mantle and core. By

Table 4*Percentage of the Observed C_{20} Potential Coefficient That Is Derived From Hydrostatic Interfaces Beneath the Lithosphere at 150-km Depth*

Model name	Compositional model	Core radius (km)	% C_{20}
DWTH	Wänke and Dreibus (1988)	1,755	4.3
DWTHC1	Wänke and Dreibus (1988)	1,805	4.5
EH45TC	Sanloup et al. (1999)	1,850	5.2
EH45TCC1	Sanloup et al. (1999)	1,718	4.9
EH45THC2	Sanloup et al. (1999)	1,795	4.6
ZGDW	Zharkov and Gudkova (2005)	1,798	5.7
DWAK	Wänke and Dreibus (1988)	1,781	6.2
LFAK	Lodders and Fegley (1997)	1,745	5.6
SAAK	Sanloup et al. (1999)	1,762	5.0
TAAK	Taylor (2013)	1,791	6.3

Note. Interior reference models are from Smrekar et al. (2019).

making assumptions about the crustal density, average thickness of the crust, and the density profile of the mantle and core, it becomes possible to invert for the relief along the crust-mantle interface and to create a map of how crustal thickness varies laterally. Crustal thickness modeling of this type has been applied to all of the terrestrial planets, the Moon, and some differentiated asteroids (see, e.g., Wicczorek, 2015). The most notable example for Mars is the work of Neumann et al. (2004), with later work by Baratoux et al. (2014) highlighting how uncertainties in the assumed crustal density affect these models.

In this section, we construct a new global crustal thickness model for Mars that takes into account explicitly the gravitational attraction of hydrostatic density interfaces beneath the lithosphere. Previously, Neumann et al. (2004) considered the gravitational contribution of the rotationally flattened core-mantle boundary. This was found to contribute 2% to the observed C_{20} potential coefficient of Mars. Later, Cheung and King (2014) improved upon this by computing the gravitational contribution of all flattened interfaces for a perfectly fluid planet before inverting for crustal thickness variations. The second-order approach of Chambat et al. (2010) was used to compute the hydrostatic gravity field in their study, but an analysis of their code shows that the contribution from the core-mantle interface was mistakenly counted twice.

In our approach, we compute the gravitational contribution resulting from all hydrostatic interfaces beneath the lithosphere. Though all harmonic degrees and orders will be considered, the largest contributor is for the C_{20} term. The predicted contribution to the observed value for this harmonic is provided in Table 4 for several density profiles that were employed in Smrekar et al. (2019). As is seen, depending on the assumed density profile, between 4.4% and 6.4% of the observed C_{20} gravity coefficient is a result of hydrostatic interfaces beneath the lithosphere. Only about 2% of the observed value is a result of the core, similar to Neumann et al. (2004), with the remainder being a result of the mantle.

We follow an approach similar to Wicczorek and Phillips (1998) for constructing a global crustal thickness model. First, the gravitational attraction of hydrostatic interfaces beneath 150-km depth was computed using the TAAK density profile, and the gravitational attraction of the surface topography was computed using an assumed density of 2,900 kg/m³. Both of these contributions were then removed from the GMM-3 gravity coefficients of Genova et al. (2016). Next, based on the TAAK reference model, a density of 3,376 kg/m³ was assigned to the uppermost mantle, and the approach of Wicczorek and Phillips (1998) was used to invert the remaining gravity field for relief along the crust-mantle interface. A downward continuation filter with an amplitude of 0.5 at degree 50 was employed, all calculations were truncated at degree 90, and gravitational finite-amplitude effects were computed to order 7, which is more than sufficient for the purposes of this work. Lacking seismic constraints, the average thickness of the crust was adjusted iteratively in order to obtain a minimum crustal thickness of 1 km, which was always found to occur in the center of the Isidis impact basin. A thicker minimum crustal-thickness constraint could have been employed, and though not considered here, lateral variations in crustal density could also have been accounted for (see Plesa et al., 2016; Smrekar et al., 2019; Wicczorek et al., 2013).

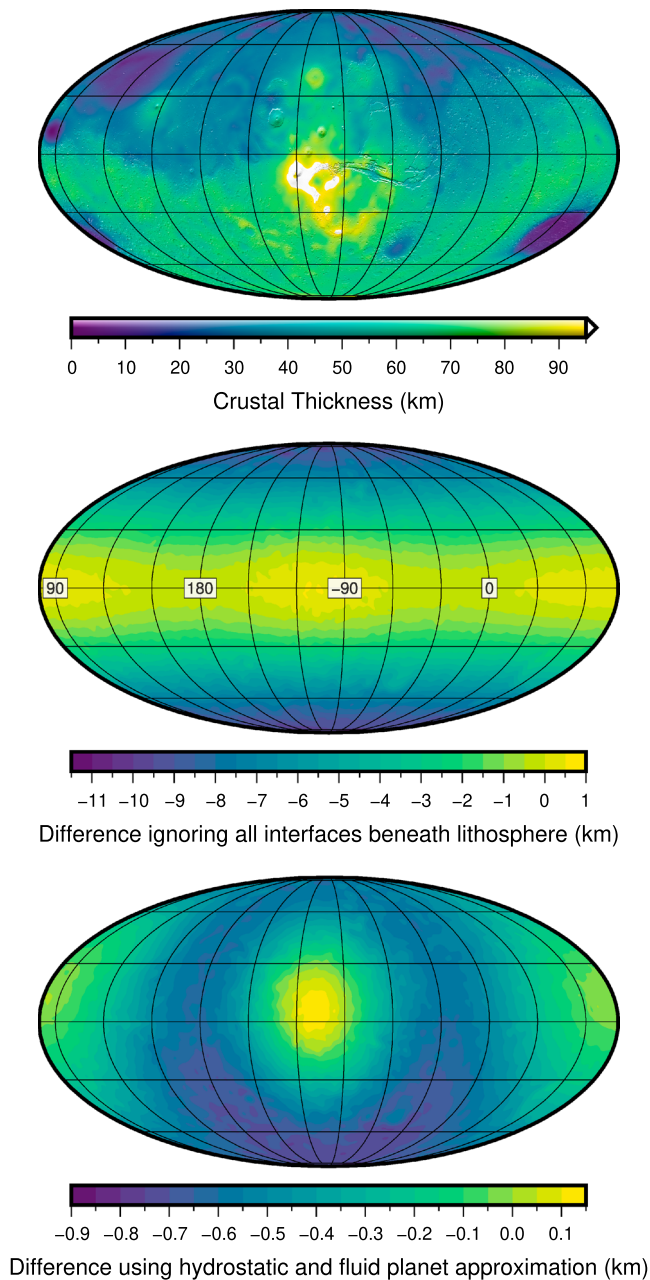


Figure 3. Crustal thickness of Mars. (top) Total crustal thickness, accounting for the gravitational attraction of hydrostatic interfaces beneath the lithosphere. (middle) Difference in crustal thickness when density interfaces beneath the lithosphere are ignored. (bottom) Difference in crustal thickness when using the hydrostatic shape of density interfaces beneath the lithosphere and the shape of these interfaces predicted for an entirely fluid planet. Images are in a Mollweide projection with a central meridian of 100° W longitude, which corresponds to the center of the Tharsis province. A shaded relief map of surface topography is overlain on the crustal thickness map in the top image. The color bars for each image are scaled to the minimum and maximum values of the data, with the exception of the top panel where the upper bound is set to 95 km.

Our final crustal thickness model is displayed in the top panel of Figure 3. For this model, the average crustal thickness is 51 km, the predicted thickness at the InSight landing site is 33 km, and the maximum thickness is 111 km. The model is broadly similar to that of Neumann et al. (2004), but as a result of including all hydrostatic interfaces beneath the lithosphere, it differs somewhat by having a different long-wavelength pole-to-equator behavior that results from a different correction to the C_{20} potential harmonic.

Table 5
Principal Moments of Inertia of the Core of Mars for the TAAK Interior Model

Moment	Fluid planet	Planet with a lithosphere
A_c	0.0254088	0.0254036
B_c	0.0254088	0.0254113
C_c	0.0255172	0.0255199

Note. The principal moments are normalized by MR^2 , where M and R are the observed mass and mean planetary radius of the planet.

The difference between our model and one that does not include any gravitational contribution from beneath the lithosphere is shown in the middle panel of this figure. The differences are small near the equator, which is a result of the fact that the minimum crustal thickness constraint occurs in the Isidis impact basin that is near the equator. However, the difference in crustal thickness grows substantially to about 11 km at the poles. In particular, at the north pole, the crustal thickness is predicted to be about 38 km when gravity contributions from beneath the lithosphere are considered and about 48 km when they are neglected. Lastly, in the bottom panel of Figure 3, we plot the difference between our crustal thickness model and one that used hydrostatic interfaces beneath the lithosphere computed for an entirely fluid planet. The differences in this case are small, with variations of only 1 km being associated with the degree-2 terms.

4.3. Mars: Free Core Nutations

The time-dependent tidal forcing exerted on the flattened shape of Mars by the Sun, planets, and Martian moons Phobos and Deimos induces periodic variations in its rotation (Dehant et al., 2000). These nutations are superposed on the much longer precession of the spin axis of the planet about the normal to the orbit plane that has a period of about 171,000 years. Since the core of Mars is at least partially fluid, relative rotational motion between the mantle and core can occur. A rotational normal mode called the free core nutation (e.g., Dehant & Mathews, 2015), describing the rotation of the core around a different spin axis than that of the solid mantle, can resonantly amplify the nutations.

Nutations of Mars will be measured by the Rotation and Interior Structure Experiment (RISE) that is part of the InSight mission (Folkner et al., 2018). The instrument measures the relative velocity between the lander and Earth from Doppler shifts of a tracking signal, and it is expected that RISE will determine the nutation period with an error of about 5 days (Folkner et al., 2018). If the shape of the core was known, the radius of the core could be constrained from the free core nutation period (Folkner et al., 2018). Conversely, if the radius of the core were known, for instance, from tidal measurements (Genova et al., 2016; Konopliv et al., 2006), seismic sounding by InSight (Panning et al., 2016), or nutation amplitude measurements by RISE (Folkner et al., 2018), the flattened shape of the core could be constrained.

Using the same reference interior model as in the previous two sections (TAAK), we have computed the three principal moments of inertia of the core, which depend upon the degree-2 core shape (see Table 5). When the core equatorial ellipticity is small compared to its polar flattening, as is the case for our model that considers gravity anomalies in the lithosphere, the frequency of the free core nutation can be expressed as (Van Hoolst & Dehant, 2002)

$$\sigma_{\text{FCN}} = -\omega \left(\frac{A}{A - A_c} \right) (\alpha_c - \tilde{\beta}). \quad (47)$$

In this equation, α_c is the dynamical flattening of the core defined as

$$\alpha_c = \frac{C_c - (A_c + B_c)/2}{(A_c + B_c)/2}. \quad (48)$$

A_c , B_c , and C_c are the three principal moments of the core, A is the minimum principal moment of the entire planet, and $\tilde{\beta} = 0.00032$ is a compliance that characterizes the core's capacity to deform due to centrifugal acceleration associated with the core rotating about a different axis than the mantle (e.g., Dehant & Mathews, 2015). We compute the moment A by use of the observed precession rate and gravity model of Konopliv et al. (2016). When normalized by MR^2 , where M is the mass of Mars and R is the mean planetary radius (3,389.5 km), we obtain $A/(MR^2)$ equal to 0.362976. We note that the first term in parentheses is insensitive

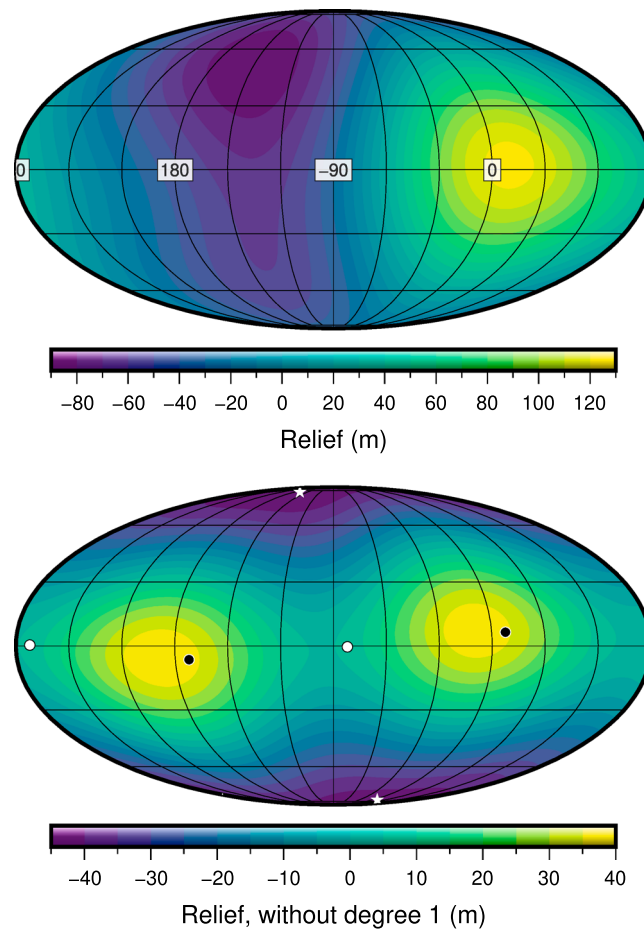


Figure 4. Relief along the core-mantle interface of the Moon with respect to a sphere of radius 330 km. The depth of the lithospheric mass anomalies was set to 34 km, and the radius of the core was set to 330 km. In the top panel, the total shape of the core is plotted, whereas in the bottom panel, the shape is plotted after removing the degree-1 terms. The axes of the A , B , and C principal moments are plotted using black circles, white circles, and stars, respectively. Images are in a Mollweide projection with a central meridian of 90° W longitude, and the color bars for each image are scaled to the minimum and maximum values of the data.

to the core shape and that the free core nutation period is linear in α_c . Equation (47) is correct up to first order in polar flattening of the core and the whole planet if the planet is biaxial (Van Hoolst et al., 2000).

The free core nutation period implied by the core figure that considers mass anomalies in the lithosphere is -232.4 days, whereas the same model using the figure of the core for a completely fluid planet is about 10 days smaller (-241.8 days). This difference is, in principle, large enough to be detected by RISE. This difference of 10 days is almost an entire consequence of the core dynamical flattening, α_c , that differs by about 3.7% between the two models. Further corrections due to triaxial effects are below 1 day (Molodensky et al., 2009; Van Hoolst & Dehant, 2002).

4.4. The Moon: Core Shape

The shape and gravity field of the Moon have long been known to be in a state that is far from hydrostatic equilibrium. Laplace (1799) was the first to note that the observed moments of inertia were inconsistent with being in hydrostatic equilibrium at the current Earth-Moon separation. Sedgwick (1898) and Jeffreys (1915) suggested that the equilibrium shape of the Moon could have been frozen into the lithosphere when the Moon was much closer to Earth in its distant past. Later studies have since attempted to quantify the lunar rotation rate, the Earth-Moon separation, and the time when this “fossil bulge” was acquired (e.g., Garrick-Bethell et al., 2006; Keane & Matsuyama, 2014; Lambeck & Pullan, 1980; Matsuyama, 2013; Qin et al., 2018). Similar to Mars, the nonhydrostatic state of the lithosphere of the Moon will generate a gravita-

Table 6
Low-Degree Spherical Harmonic Coefficients (in Meters) of the Relief Along the Core-Mantle Interface of the Moon

l	m	h_{lm}	$h_{l,-m}$
0	0	330,000	
1	0	−5.98	
1	1	49.16	20.45
2	0	−18.93	
2	1	4.64	0.09
2	2	8.46	−2.47
3	0	−0.20	
3	1	0.55	0.14
3	2	0.15	0.01
3	3	0.10	−0.06

Note. The lithospheric mass anomalies were placed at a depth of 34 km, and the core radius is 330 km.

tional potential that will affect the shapes of hydrostatic interfaces at depth. In this section, we address how the lithospheric gravity field affects the shape of the lunar core.

Two studies have noted previously that the shape of the core of the Moon is likely to be different from that expected for an entirely fluid body. In a study of the precession of the lunar core, Meyer and Wisdom (2011) calculated the core flattening by taking into account the potential arising from a “nonhydrostatic mantle.” One of the two methods used to solve for the h_{20} core shape was similar in spirit to the method outlined in section 2. They found that the present-day core flattening was about 10 times greater than that predicted for an entirely fluid body and that the predicted value was consistent with that inferred from analyses of LLR data (Williams et al., 2014). In a different study, the fluid dynamics of the core following large impact events was investigated by Le Bars et al. (2011). In this model, inertial instabilities in the core were excited by differential rotation at a triaxial core-mantle interface, allowing for the generation of a short-lived dynamo. Using an approach derived from that described here, both the core flattening and equatorial ellipticity were computed by taking into account the gravitational potential of the lithosphere.

We here compute the predicted hydrostatic shape of the lunar core for all harmonics up to degree 15. A range of values for the mean core radius is used, given that the core radius and density are not well constrained by seismic data (Garcia et al., 2011; Weber et al., 2011). For each core radius, the core and mantle densities were determined in order to simultaneously fit both the total mass of the Moon and the mean moment of inertia of the solid portion of the Moon as quoted in Williams et al. (2014). Following Wiczorek et al. (2013), a mean crustal density of 2,550 kg/m³ was adopted, and mean crustal thicknesses of 34 and 43 km were considered. The lithospheric mass anomalies were assumed to be located at the mean depth of the crust-mantle interface, and the degree 900 gravity model 900C11A of Konopliv et al. (2014) was used when calculating the hydrostatic shape of the core. For the shape of the surface, we use the principal axis referenced spherical harmonic model LOLA1500p of Wiczorek (2015).

The shape of the core is plotted in Figure 4 for the case of a 34-km-thick crust and a 330-km core radius. As is shown in the upper image, the relief along the core varies from about −90 to 130 m. In comparison, if the Moon were entirely fluid, only about 5 m of relief would be expected. This image shows that the largest contribution to the core shape comes from the degree-1 terms (see also the spherical harmonic coefficients in Table 6). In particular, the amplitude of the degree-1 relief is 93 m, which implies that the center of the core is offset from the center-of-mass of the Moon by the same amount. We note that the amplitude of the degree-1 relief along the core-mantle boundary of the Moon is nearly the same as that for Mars. Nevertheless, given that the degree-2 components of the core shape of Mars are considerably larger than for the Moon, the degree-1 relief of Mars is not as apparent in Figure 2 as it is for the Moon in Figure 4.

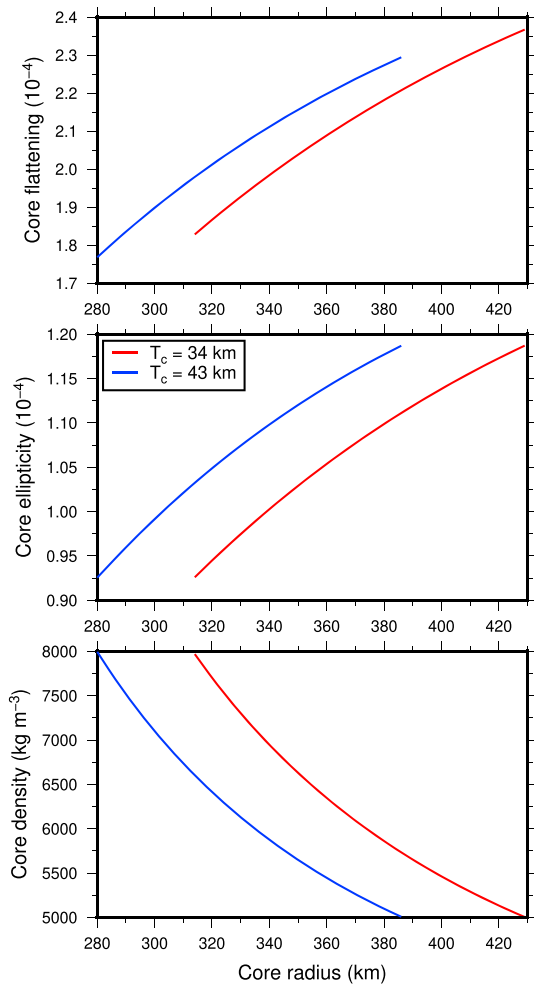


Figure 5. Core flattening, core equatorial ellipticity, and core density as a function of core radius. Each model satisfies the mean moment of inertia of the Moon, the depth of the lithospheric mass anomalies is set to the depth of the crust-mantle interface, and two different crustal thicknesses of 34 and 43 km are considered.

In the bottom image of this figure, we plot the core shape after removing the contribution of the degree-1 terms. Here we see that there is still significant relief that varies from about -45 to 40 m. Though this relief corresponds approximately to a triaxial ellipsoid, the core shape has non-negligible h_{21} , $h_{2,-1}$, and $h_{2,-2}$ terms, implying that the core shape is not, in fact, perfectly aligned with the Moon's principal moments. In particular, the maximum moment C is inclined with respect to the rotation axis by about 6.4° , and the minimum moment A passes through 7.9° W longitude. As shown in Table 6, the shape of the core also has a small contribution from the degree-3 terms, and these are expected to affect the rotation dynamics of the Moon as seen by LLR data (e.g., Williams et al., 2001). We note that if the crustal thickness was increased from 34 to 43 km, then the relief along the core would change by a maximum of 26 m.

The degree-2 characteristics of the core shape are summarized in Figure 5 for the range of possible core radii. In the lower image, the relations between core density and radius are plotted, which are determined by fitting the mass and moment-of-inertia constraints. The minimum possible core radius is seen to be about 280 km, and we note that seismic estimates range from 330 ± 20 km (Weber et al., 2011) to 380 ± 40 km (Garcia et al., 2011). The upper two panels plot the core flattening, f , and equatorial ellipticity, β , defined as

$$f = \frac{(a+b)/2 - c}{c}, \quad (49)$$

$$\beta = \frac{a^2 - b^2}{a^2 + b^2}, \quad (50)$$

where a , b , and c are the core radii along the directions of the core principal moments. Allowable values of the flattening are in the range $(1.75\text{--}2.35) \times 10^{-4}$, which are about 10% smaller than those presented in Meyer and Wisdom (2011). The main cause of this slight difference is that they used only a single interface at the surface of the planet for the lithosphere, whereas our approach used the observed topography and an additional interface at the crust-mantle interface.

For a 34-km-thick crust and 330-km core radius, the present-day core flattening is computed to be 2.06×10^{-4} , which is consistent with the LLR-derived value of $(2.46 \pm 1.4) \times 10^{-4}$ (Williams et al., 2014). Nevertheless, it should be noted that a subsequent analysis of the LLR data by Williams and Boggs (2015) suggested that the core flattening detection is equivocal given uncertainties in the frequency dependence of the k_2 Love number. The equatorial ellipticity is plotted in the middle panel of Figure 5, where the present-day values have the range $(0.9\text{--}1.2) \times 10^{-4}$. Our computed values are consistent with those reported by Le Bars et al. (2011) and are about 5 times greater than would be expected for an entirely fluid planet.

5. Summary and Conclusions

There is a long history of calculating the shapes and gravity fields of the rocky planets, moons, and dwarf planets under the assumption that they are in hydrostatic equilibrium. These objects, however, all possess a strong lithosphere, which is inconsistent with the underlying assumption of these studies. In this work, we have investigated the case where an object is instead hydrostatic only beneath the lithosphere and where mass anomalies in the lithosphere perturb the shapes of hydrostatic density interfaces. A first-order theory was developed that considers both rotational and tidal potentials, the known gravity field of the body, and an assumed discretized radial density profile. The shapes of the hydrostatic interfaces are determined by solution of a simple matrix equation, and for the case of an entirely fluid rotating body, our approach is

shown to be more accurate than previous first-order theories as a result of including additional small terms related to the rotational potential.

As applications of our approach, we have computed the shapes of hydrostatic interfaces in both Mars and the Moon. The planet Mars has significant variations in the height of its geoid as a result of mass anomalies associated with the Tharsis volcanic province. Up to 3 km of geoid relief is present at the surface with respect to the shape predicted for an entirely fluid planet. Just beneath the lithosphere, hydrostatic interfaces are perturbed by almost 2 km, and even at the core-mantle boundary, more than 700 m of additional relief is predicted to present. The perturbation of the degree-2 shape of the core modifies the free core nutation period by about 10 days. As a result of degree-1 mass anomalies at the surface and in the lithosphere, we find that the core should be offset from the center of mass of the planet by almost 90 m. Depending on the assumed density profile, the gravitational attraction of the hydrostatic interfaces can contribute from about 4% to 6% to the observed spherical-harmonic zonal degree-2 gravity coefficient. If the gravitational attraction of the hydrostatic interfaces were neglected entirely when computing a crustal-thickness map, long-wavelength biases of about 12 km would arise.

The long-wavelength shape of the Moon is also far from hydrostatic equilibrium. In contrast to Mars, whose shape of the core-mantle boundary is largely described by spherical harmonics of degree 2, the dominant shape of the lunar core is of spherical harmonic degree 1. The core is predicted to be offset by more than 90 m from the center of mass of the Moon, and spherical harmonic degree-2 terms contribute additional relief with an amplitude of about 40 m. As shown previously, the flattening (Meyer & Wisdom, 2011) and equatorial ellipticity (Le Bars et al., 2011) of the core are predicted to be about 10 and 5 times larger, respectively, than for an entirely fluid body. Both the degree-2 and degree-3 shapes of the lunar core are important for the interpretation of LLR data.

We have discussed here only a few of the potential applications of our work for Mars and the Moon. Many other applications are possible, as the technique can be applied to any planetary object that has a lithosphere, and whose low-degree gravity field is known. In addition to Mars and the Moon, such objects include Mercury, Venus, Earth, dwarf planets like Vesta and Ceres, and the icy satellites of Jupiter and Saturn.

Acknowledgments

The authors thank two anonymous reviewers for comments that helped improve the clarity of the manuscript. The authors also thank Nicolas Rambaux, Adrian Broquet, Francis Nimmo, Tamara Gudkova, and Scott King for the comments and discussions that helped improve this paper. M. A. W. was supported by the French space agency, CNES (Centre National d'Etudes Spatiales). M. B., A. R., and T. V. H. were financially supported by the Belgian PRODEX program managed by ESA in collaboration with the Belgian Federal Science Policy Office. Calculations were performed using the `pyshools` software package (Wieczorek & Meschede, 2018), and scripts to reproduce the figures can be found in the lead author's `pycrust` GitHub repository (<https://github.com/MarkWieczorek/pyCrust>). This is InSight contribution number 89.

References

- Baland, R. M., Tobie, G., Lefèvre, A., & Hoolst, T. V. (2014). Titan's internal structure inferred from its gravity field, shape, and rotation state. *Icarus*, *237*, 29–41. <https://doi.org/10.1016/j.icarus.2014.04.007>
- Baratoux, D., Samuel, H., Michaut, C., Toplis, M. J., Monnerieu, M., Wieczorek, M., & Kurita, K. (2014). Petrological constraints on the density of the Martian crust. *Journal of Geophysical Research: Planets*, *119*, 1707–1727. <https://doi.org/10.1002/2014JE004642>
- Beuthe, M., Rivoldini, A., & Trinh, A. (2016). Enceladus's and Dione's floating ice shells supported by minimum stress isostasy. *Geophysical Research Letters*, *43*, 10,088–10,096. <https://doi.org/10.1002/2016GL070650>
- Blakely, R. J. (1995). *Potential theory in gravity and magnetic applications*. New York: Cambridge Univ. Press.
- Chambat, F., Ricard, Y., & Valette, B. (2010). Flattening of the Earth: Further from hydrostaticity than previously estimated. *Geophysical Journal International*, *183*, 727–732. <https://doi.org/10.1111/j.1365-246X.2010.04771.x>
- Chandrasekhar, S. (1969). *Ellipsoidal figures of equilibrium*. New York: Dover Publications.
- Cheung, K. K., & King, S. D. (2014). Geophysical evidence supports migration of Tharsis volcanism on Mars. *Journal of Geophysical Research: Planets*, *119*, 1078–1085. <https://doi.org/10.1002/2014JE004632>
- Clairaut, A. C. (1743). *Théorie de la figure de la Terre, Tirée des principes de l'hydrostatique*. Paris: David Fils and Durand.
- Defraigne, P., Dehant, V., & Van Hoolst, T. (2001). Steady-state convection in Mars-mantle. *Planetary and Space Science*, *49*, 501–509. [https://doi.org/10.1016/S0032-0633\(00\)00142-2](https://doi.org/10.1016/S0032-0633(00)00142-2)
- Dehant, V., Defraigne, P., & Van Hoolst, T. (2000). Computation of Mars' transfer functions for nutations, tides and surface loading. *Physics of the Earth and Planetary Interiors*, *117*, 385–395. [https://doi.org/10.1016/S0031-9201\(99\)00108-9](https://doi.org/10.1016/S0031-9201(99)00108-9)
- Dehant, V., & Mathews, P. M. (2015). *Precession, nutation and wobble of the Earth*. Cambridge: Cambridge University Press.
- Dumberry, M., Rivoldini, A., Van Hoolst, T., & Yseboodt, M. (2013). Role of Mercury's core density structure on its longitudinal librations. *Icarus*, *225*, 62–74. <https://doi.org/10.1016/j.icarus.2013.03.001>
- Dumberry, M., & Wieczorek, M. A. (2016). The forced precession of the Moon's inner core. *Journal of Geophysical Research: Planets*, *121*, 1264–1292. <https://doi.org/10.1002/2015JE004986>
- Ermakov, A. I., Fu, R. R., Castillo-Rogez, J. C., Raymond, C. A., Park, R. S., Preusker, F., & Zuber, M. T. (2017). Constraints on Ceres' internal structure and evolution from its shape and gravity measured by the Dawn spacecraft. *Journal of Geophysical Research: Planets*, *122*, 2267–2293. <https://doi.org/10.1002/2017JE005302>
- Folkner, W. M., Dehant, V., Le Maistre, S., Yseboodt, M., Rivoldini, A., Van Hoolst, T., & Golombek, M. P. (2018). The Rotation and Interior Structure Experiment on the InSight Mission to Mars. *Space Science Reviews*, *214*(5), 100. <https://doi.org/10.1007/s11214-018-0530-5>
- García, R., Gagnepain-Beyneix, J., Chevrot, S., & Lognonné, P. (2011). Very preliminary reference Moon model. *Physics of the Earth and Planetary Interiors*, *188*, 96–113. <https://doi.org/10.1016/j.pepi.2011.06.015>
- Garrick-Bethell, I., Wisdom, J., & Zuber, M. T. (2006). Evidence for a past high-eccentricity lunar orbit. *Science*, *313*, 652–655. <https://doi.org/10.1126/science.1128237>

- Genova, A., Goossens, S., Lemoine, F. G., Mazarico, E., Neumann, G. A., Smith, D. E., & Zuber, M. T. (2016). Seasonal and static gravity field of Mars from MGS, Mars Odyssey and MRO radio science. *Icarus*, *272*, 228–245. <https://doi.org/10.1016/j.icarus.2016.02.050>
- Hoolst, T. V., Baland, R. M., & Trinh, A. (2016). The diurnal libration and interior structure of Enceladus. *Icarus*, *277*, 311–318. <https://doi.org/10.1016/j.icarus.2016.05.025>
- Hubbard, W. B. (2013). Concentric Maclaurin spheroid models of rotating liquid planets. *The Astrophysical Journal*, *768*, 1–8. <https://doi.org/10.1088/0004-637X/768/1/43>
- Iess, L., Rappaport, N. J., Jacobson, R. A., Stevenson, P. R. D. J., Tortora, P., Armstrong, J. W., & Asmar, S. W. (2010). Gravity field, shape, and moment of inertia of Titan. *Science*, *327*, 1367–1369. <https://doi.org/10.1126/science.1182583>
- Jeffreys, H. (1915). Certain hypothesis as to the internal structure of the Earth and Moon. *Memoirs of the Royal Astronomical Society*, *60*, 187–217.
- Jeffreys, H. (1970). *The Earth* (5th ed.). Cambridge: Cambridge University Press.
- Keane, J. T., & Matsuyama, I. (2014). Evidence for lunar true polar wander and a past low-eccentricity, synchronous lunar orbit. *Geophysical Research Letters*, *41*, 6610–6619. <https://doi.org/10.1002/2014GL061195>
- Konopliv, A. S., Park, R. S., & Folkner, W. M. (2016). An improved JPL Mars gravity field and orientation from Mars orbiter and lander tracking data. *Icarus*, *274*, 253–260. <https://doi.org/10.1016/j.icarus.2016.02.052>
- Konopliv, A. S., Park, R. S., Yuan, D. N., Asmar, S. W., Watkins, M. M., Williams, J. G., & Zuber, M. T. (2014). High resolution lunar gravity fields from the GRAIL primary and extended mission. *Geophysical Research Letters*, *41*, 1452–1458. <https://doi.org/10.1002/2013GL059066>
- Konopliv, A. S., Yoder, C. F., Standish, E. M., Yuan, D. N., & Sjogren, W. L. (2006). A global solution for the Mars static and seasonal gravity, Mars orientation, Phobos and Deimos masses, and Mars ephemeris. *Icarus*, *182*, 23–50. <https://doi.org/10.1016/j.icarus.2005.12.025>
- Kopal, Z. (1960). *Figures of equilibrium of celestial bodies with emphasis on problems of motion of artificial satellites*. Madison: Univ. Wisconsin Press.
- Lambeck, K., & Pullan, S. (1980). The lunar fossil bulge hypothesis revisited. *Physics of the Earth and Planetary Interiors*, *22*, 29–35. [https://doi.org/10.1016/0031-9201\(80\)90097-7](https://doi.org/10.1016/0031-9201(80)90097-7)
- Lanzano, P. (1982). *Deformations of an elastic Earth*. New York: Academic Press.
- Laplace, P. S. (1799). *Traité de Mécanique céleste* (Vol. 2). Paris: Crapelet.
- Le Bars, M., Wieczorek, M., Karatekin, O., Cébron, D., & Laneuville, M. (2011). An impact-driven dynamo for the early Moon. *Nature*, *479*, 215–218. <https://doi.org/10.1038/nature10565>
- Lefevre, A., Tobie, G., Choblet, G., & Cadek, O. (2014). Structure and dynamics of Titan's outer icy shell constrained by Cassini data. *Icarus*, *237*, 16–28. <https://doi.org/10.1016/j.icarus.2014.04.006>
- Lodders, K., & Fegley, B. (1997). An oxygen isotope model for the composition of Mars. *Icarus*, *126*, 373–394. <https://doi.org/10.1006/icar.1996.5653>
- Lognonné, P., Banerdt, W. B., Giardini, D., Pike, W. T., Christensen, U., Laudet, P., & Wookey, J. (2019). SEIS: Insight's seismic experiment for internal structure of Mars. *Space Science Reviews*, *215*, 12. <https://doi.org/10.1007/s11214-018-0574-6>
- Matsuyama, I. (2013). Fossil figure contribution to the lunar figure. *Icarus*, *222*, 411–414. <https://doi.org/10.1016/j.icarus.2012.10.025>
- McKinnon, W. B. (2013). The shape of Enceladus as explained by an irregular core: Implications for gravity, libration, and survival of its subsurface ocean. *Journal of Geophysical Research: Planets*, *118*, 1775–1788. <https://doi.org/10.1002/jgre.20122>
- Meyer, J., & Wisdom, J. (2011). Precession of the lunar core. *Icarus*, *211*, 921–924. <https://doi.org/10.1016/j.icarus.2010.09.016>
- Molodensky, S. M., Zharkov, V. N., & Gudkova, T. V. (2009). On models of Mars' interior and amplitudes of forced nutations 2. The effects of liquid core and mantle elasticity. *Physics of the Earth and Planetary Interiors*, *172*, 335–344. <https://doi.org/10.1016/j.pepi.2008.10.008>
- Nakiboglu, S. M. (1982). Hydrostatic theory of the Earth and its mechanical implications. *Physics of the Earth and Planetary Interiors*, *28*, 302–311. [https://doi.org/10.1016/0031-9201\(82\)90087-5](https://doi.org/10.1016/0031-9201(82)90087-5)
- Neumann, G. A., Zuber, M. T., Wieczorek, M. A., McGovern, P. J., Lemoine, F. G., & Smith, D. E. (2004). Crustal structure of Mars from gravity and topography. *Journal of Geophysical Research*, *109*, E08002. <https://doi.org/10.1029/2004JE002262>
- Panning, M. P., Lognonné, P., Bruce Banerdt, W., Garcia, R., Golombek, M., Kedar, S., & Wookey, J. (2016). Planned products of the Mars structure service for the InSight Mission to Mars. *Space Science Reviews*, *211*, 611–650. <https://doi.org/10.1007/s11214-016-0317-5>
- Park, R. S., Konopliv, A. S., Bills, B. G., Rambaux, N., Castillo-Rogez, J. C., Raymond, C. A., & Preusker, F. (2016). A partially differentiated interior for (1) Ceres deduced from its gravity field and shape. *Nature*, *537*, 515–517. <https://doi.org/10.1038/nature18955>
- Phillips, R. J., Zuber, M. T., Smrekar, S. E., Mellon, M. T., Head, J. W., Tanaka, K. L., & Marinangeli, L. (2001). Mars north polar deposits: Stratigraphy, age, and geodynamical response. *Science*, *320*, 1182–1185. <https://doi.org/10.1126/science.1157546>
- Phillips, R. J., Zuber, M. T., Solomon, S. C., Golombek, M. P., Jakosky, B. M., & Banerdt, W. B. IIS. A. H. (2001). Ancient geodynamics and global-scale hydrology on Mars. *Science*, *291*, 2587–2591. <https://doi.org/10.1126/science.1058701>
- Plesa, A. C., Grott, M., Tosi, N., Breuer, D., Spohn, T., & Wieczorek, M. A. (2016). How large are present-day heat flux variations across the surface of Mars? *Journal of Geophysical Research: Planets*, *121*, 2386–2403. <https://doi.org/10.1002/2016JE005126>
- Qin, C., Zhong, S., & Phillips, R. (2018). Formation of the lunar fossil bulges and its implication for the early Earth and Moon. *Geophysical Research Letters*, *45*, 1286–1296. <https://doi.org/10.1002/2017GL076278>
- Rambaux, N., Chambat, F., & Castillo-Rogez, J. C. (2015). Third-order development of shape, gravity and moment of inertia for highly flattened celestial bodies. Application to Ceres. *Astronomy & Astrophysics*, *585*, A127. <https://doi.org/10.1051/0004-6361/201527005>
- Romanowicz, B. (2003). Global mantle tomography: Progress status in the last 10 years. *Annual Review Geophysics Space Physical*, *31*, 303–333. <https://doi.org/10.1146/annurev.earth.31.091602.113555>
- Sanloup, C., Jambon, A., & Gillet, P. (1999). A simple chondritic model of Mars. *Physics of the Earth and Planetary Interiors*, *112*, 43–54. [https://doi.org/10.1016/S0031-9201\(98\)00175-7](https://doi.org/10.1016/S0031-9201(98)00175-7)
- Schubert, G., Anderson, J. D., Spohn, T., & McKinnon, W. B. (2004). Interior composition, structure and dynamics of the Galilean satellites. In F. Bagenal, T. E. Dowling, & W. B. McKinnon (Eds.), *Jupiter* (pp. 281–306). Cambridge: Cambridge University Press.
- Sedgwick, W. F. (1898). On the figure of the Moon. *Messenger Math*, *27*, 171–173.
- Smith, D. E., Sjogren, W. L., Tyler, G. L., Balmino, G., Lemoine, F. G., & Konopliv, A. S. (1999). The gravity field of Mars: Results from Mars Global Surveyor. *Science*, *286*, 94–97. <https://doi.org/10.1126/science.286.5437.94>
- Smrekar, S., Lognonné, P., Spohn, T., Banerdt, B., Breuer, D., Christensen, U., & Wieczorek, M. (2019). Pre-Mission InSights on the interior of Mars. *Space Science Reviews*, *215*, 3. <https://doi.org/10.1007/s11214-018-0563-9>
- Taylor, G. J. (2013). The bulk composition of Mars. *Chemie der Erde*, *73*, 401–420. <https://doi.org/10.1016/j.chemer.2013.09.006>
- Van Hoolst, T., & Dehant, V. (2002). Influence of triaxiality and second-order terms in flattenings on the rotation of terrestrial planets: I. Formalism and rotational normal modes. *Physics of the Earth and Planetary Interiors*, *134*(1), 17–33. [https://doi.org/10.1016/S0031-9201\(02\)00068-7](https://doi.org/10.1016/S0031-9201(02)00068-7)

- Van Hoolst, T., Dehant, V., & Defraigne, P. (2000). Sensitivity of the free core nutation and the Chandler wobble to changes in the interior structure of Mars. *Physics of the Earth and Planetary Interiors*, 117, 397–405. [https://doi.org/10.1016/S0031-9201\(99\)00109-0](https://doi.org/10.1016/S0031-9201(99)00109-0)
- Wänke, H., & Dreibus, G. (1988). Chemical composition and accretion history of terrestrial planets. *Philosophical Transactions of the Royal Society A*, 325, 545–557. <https://doi.org/10.1098/rsta.1988.0067>
- Weber, R. C., Lin, P. Y., Garnero, E. J., Williams, Q., & Lognonné, P. (2011). Seismic detection of the lunar core. *Science*, 331, 309–312. <https://doi.org/10.1126/science.1199375>
- Wieczorek, M. A. (2008). Constraints on the composition of the martian south polar cap from gravity and topography. *Icarus*, 196, 506–517. <https://doi.org/10.1016/j.icarus.2007.10.026>
- Wieczorek, M. A. (2015). Gravity and topography of the terrestrial planets. In T. Spohn, & G. Schubert (Eds.), *Treatise on geophysics (second edition)* (Vol. 10, pp. 153–193). Oxford: Elsevier-Perigamon. <https://doi.org/10.1016/B978-0-444-53802-4.00169-X>
- Wieczorek, M. A., & Meschede, M. (2018). SHTools: Tools for working with spherical harmonics. *Geochemistry, Geophysics, Geosystems*, 19, 2574–2592. <https://doi.org/10.1029/2018GC007529>
- Wieczorek, M. A., Neumann, G. A., Nimmo, F., Kiefer, W. S., Taylor, G. J., Melosh, H. J., & Zuber, M. T. (2013). The crust of the Moon as seen by GRAIL. *Science*, 339(6120), 671–675. <https://doi.org/10.1126/science.1231530>
- Wieczorek, M. A., & Phillips, R. J. (1998). Potential anomalies on a sphere: Applications to the thickness of the lunar crust. *Journal of Geophysical Research*, 103(E1), 1715–1724. <https://doi.org/10.1029/97JE03136>
- Wieczorek, M. A., & Zuber, M. T. (2004). Thickness of the Martian crust: Improved constraints from geoid-to-topography ratios. *Journal of Geophysical Research*, 109, E01009. <https://doi.org/10.1029/2003JE002153>
- Williams, J. G., & Boggs, D. H. (2015). Tides on the Moon: Theory and determination of dissipation. *Journal of Geophysical Research: Planets*, 120, 689–724. <https://doi.org/d10.1002/2014JE004755>
- Williams, J. G., Boggs, D. H., Yoder, C. F., Ratcliff, J. T., & Dickey, J. O. (2001). Lunar rotational dissipation in solid body and molten core. *Journal of Geophysical Research*, 106, 27,933–27,968. <https://doi.org/10.1029/2000JE001396>
- Williams, J. G., Konopliv, A. S., Boggs, D. H., Park, R. S., Yuan, D. N., Lemoine, F. G., & Zuber, M. T. (2014). Lunar interior properties from the GRAIL mission. *Journal of Geophysical Research: Planets*, 119, 1546–1578. <https://doi.org/10.1002/2013JE004559>
- Wisdom, J., & Hubbard, W. B. (2016). Differential rotation in Jupiter: A comparison of methods. *Icarus*, 267, 315–322. <https://doi.org/10.1016/j.icarus.2015.12.030>
- Wu, X., & Wahr, J. M. (1997). Effects of non-hydrostatic core-mantle boundary topography and core dynamics on Earth rotation. *Geophysical Journal International*, 128, 18–42. <https://doi.org/10.1111/j.1365-246X.1997.tb04069.x>
- Zharkov, V. N., & Gudkova, T. V. (2005). Construction of Martian interior model. *Solar System Research*, 39, 343–373. <https://doi.org/10.1007/s11208-005-0049-7>
- Zharkov, V. N., Gudkova, T. V., & Molodensky, S. M. (2009). On models of Mars' interior and amplitudes of forced nutations 1. The effects of deviation of Mars from its equilibrium state on the flattening of the core-mantle boundary. *Physics of the Earth and Planetary Interiors*, 172, 324–334. <https://doi.org/10.1016/j.pepi.2008.10.009>
- Zharkov, V. N., & Trubitsyn, V. P. (1978). *Physics of planetary interiors*. Tucson: Pachart Publishing House.